Antiferromagnetic Cavity Magnon Polaritons in Collinear and Canted Phases of Hematite

I. Boventer,[1,*] H. T. Simensen,[2] B. Brekke,[2] M. Weides,[3] A. Anane,[1] M. Kläui,[2,4,5] A. Brataas,[2] and R. Lebrun[1,†]

[1] *Unité Mixte de Physique CNRS, Thales, Université Paris-Saclay, Palaiseau 91767, France*

[2] *Center for Quantum Spintronics, Department of Physics, Norwegian University of Science and Technology, Trondheim NO-7491, Norway*

[3] *James Watt School of Engineering, Electronics & Nanoscale Engineering Division, University of Glasgow, Glasgow G12 8QQ, United Kingdom*

[4] *Institut für Physik, Johannes-Gutenberg-Universität Mainz, D-55099, Mainz, Germany*

[5] *Graduate School of Excellence Materials Science in Mainz (MAINZ), Staudinger Weg 9, D-55128, Mainz, Germany*

(Received 16 December 2021; revised 5 December 2022; accepted 7 December 2022; published 30 January 2023)

Cavity spintronics explores light-matter interactions at the interface between spintronic and quantum phenomena. Until now, studies have focused on the hybridization between magnons in ferromagnets and cavity photons. Here, we realize antiferromagnetic cavity magnon polaritons. Hybridization arises from the interaction of the collective spin motion in single hematite crystals (α-Fe_2O_3) and the microwave field of integrated cavities operating between 18 and 45 GHz. We show theoretically and experimentally that the photon-magnon coupling in the collinear phase is mediated by the dynamic Néel vector and the weak magnetic moment in the canted phase by measuring across the Morin transition. We show that the coupling strength, $\tilde{g}$, scales with the anisotropy field in the collinear phase and with the Dzyaloshinskii-Moriya field in the canted phase. We reach the strong-coupling regime in both canted (cooperativity $C > 70$ for selected modes at 300 K) and noncollinear phases ($C > 4$ at 150 K), and thus, towards coherent information-exchange-harnessing antiferromagnetic cavity magnon polaritons. These results provide evidence for a generic strategy to achieve cavity magnon polaritons in antiferromagnets for different symmetries, opening the field of cavity spintronics to antiferromagnetic materials.

DOI: 10.1103/PhysRevApplied.19.014071

I. INTRODUCTION

The generation [1–4] and manipulation [5,6] of cavity magnon polaritons (CMPs) and exploring the strategies to integrate them into devices is at the core of cavity spintronics. The CMP is a quasiparticle associated with the hybridization of a cavity photon and a magnon, the quanta of a spin wave [7,8]. Research directions in cavity magnonics range from studies on quantum information processing [9–12] to long-distance transport of spin current via cavities [13] and optomagnonics [14–16]. The hybrid nature of a CMP allows for its interconnection with (nonlinear) physical systems, such as superconducting qubits, leading to quantum magnonics [17–19]. In parallel, the possibility of achieving coherent or dissipative coupling regimes, and non-Hermitian systems, can enable the development of nonreciprocal information processing [5,6,20,21]. A coherent transfer of information [17,20–23] is achieved when $\tilde{g} \gg \kappa_c, \kappa_m$. Then, the macroscopic coupling strength, $\tilde{g}$, exceeds the dissipation parameters (the cavity-resonator linewidth, κ_c, and the magnon linewidth, κ_m). The associated experimental hallmark is observing an avoided level crossing.

Cavity magnonics mainly focuses on ferromagnetic (FM) materials, and especially on yttrium iron garnet (YIG), which exhibits the lowest known Gilbert damping in ferromagnetic materials [17,24–26]. Antiferromagnetic (AFM) materials possess higher-frequency modes that can reach the terahertz (THz) range and have, in recent years, been at the heart of intense research on spintronics [27–29]. Furthermore, AFM materials can exhibit various magnetic configurations, ranging from collinear easy-axis and

*isabella.boventer@cnrs-thales.fr

†romain.lebrun@cnrs-thales.fr

easy-plane ordering to noncollinear spin textures. Recent research highlights that some insulating antiferromagnets also possess ultralow magnetic damping, leading to long-distance spin transport [30–34]. However, antiferromagnetic materials often couple weakly to external excitations due to vanishing stray fields. Thus, the hybridization of AFM magnons with cavity photons remains largely unexplored, with only a few recent experimental reports at millikelvin and sub-THz frequencies [35–39] that do not directly study the nature of the coupling regime. The development of antiferromagnetic cavity magnonics thus requires solving two key bottlenecks. On the fundamental side, it requires an understanding of how cavity photons can efficiently couple with the dynamics of the Néel order in compensated AFMs and in canted AFMs, potentially with their weak canted moments. On the applied side, it requires a demonstration of an easily accessible strong-coupling regime. In turn, the latter enables the development of other nonlinear components for nonreciprocal information processing and quantum cavity magnonics, together with future downscaling to on-chip platforms.

This article explores antiferromagnetic cavity photon magnon polaritons (ACMPs) and their associated dynamics in collinear and noncollinear antiferromagnets using the model antiferromagnet hematite (α-Fe_2O_3) below and above the Morin transition ($T_{\text{Morin}} \sim 260$ K [40]). We demonstrate both theoretically and experimentally that the coupling strength, $\tilde{g(T)}$, scales as $(H_{A'}(T)/8H_E)^{1/4}$ [41] in the collinear phase and as $\sqrt{2\gamma(H_D+H_0)^2/\omega_0 H_E}$ in the noncollinear phase ($H_{A'}$, easy-axis anisotropy field; H_E, exchange field; H_D, Dzyaloshinskii-Moriya field; and H_0, applied magnetic field). In the canted phase of hematite, we find an efficiency only about 20 smaller than that in the ferromagnet YIG [sphere ($\varnothing = 1$ mm)]. We report the creation of ACMPs in a frequency range of 18–45 GHz both with the right-handed low-frequency mode in the canted easy-plane (CEP) phase ($T = 300$ K) and with the left-handed mode below the Morin transition in the collinear easy-axis (EA) phase. Due to the low magnetic damping of hematite, κ_m, and a low cavity linewidth, κ_c, compared to the coupling strength, we obtain a cooperativity of $C = \tilde{g}^2/(\kappa_c\kappa_m) > 1$, in both the EA ($C > 4$) and CEP phases ($C > 70$). Our findings demonstrate a persistent coherent information exchange between cavity-resonator photons and antiferromagnetic magnons for all temperatures and two different AFM configurations.

II. THEORETICAL MODEL

We first model the coupling of a cavity-resonator mode with an AFM magnon mode using the system Hamiltonian $\mathcal{H}_{\text{sys}} = \mathcal{H}_c + \mathcal{H}_{\text{AFM}} + \mathcal{H}_{\text{CAFM}}$, with $\mathcal{H}_c$, $\mathcal{H}_{\text{AFM}}$, and $\mathcal{H}_{\text{CAFM}}$, respectively, describing the cavity photons, the antiferromagnetic magnons and the cavity photon-magnon coupling (cf. Appendix B):

$$\mathcal{H}_{\text{sys}} = \hbar\omega_c\, aa^\dagger + \hbar\omega_m mm^\dagger + \hbar\,\tilde{g}(m^\dagger a + a^\dagger m), \qquad (2)$$

where ω_c and ω_m, respectively, correspond to the cavity photon and AFM magnon frequencies; and $\tilde{g}$ is the macroscopic coupling strength of the cavity photons with the AFM magnons. Importantly, $\tilde{g}$ also scales as $g_0\sqrt{2NS}$, with $g_0 = (\eta|\gamma|/2)\sqrt{\hbar\omega_0\mu_0/2V_m}$ being the single-spin coupling strength (ω_0, resonance frequency of the polariton, where $\omega_c = \omega_m \equiv \omega_0$; V_m, cavity-mode volume) and NS corresponding to the total spin numbers involved in the coupling (S, spin number). The dimensionless factor η accounts for the (spatial) mode overlap between the cavity photons and the magnons [41]. In AFMs, the expression of $\tilde{g}$ also depends on the AFM configuration (easy-axis or easy-plane) and requires distinguishing between collinear and noncollinear cases. In Table I, we present the derived effective coupling strength for both collinear easy-axis AFMs [41] and canted antiferromagnets (see Appendix B).

For collinear easy-axis AFMs, ACMPs originate from the strong coupling of the cavity photons with the dynamics [$\propto (H_{A'}/8H_E)^{1/4}$] of the compensated Néel vector [Eq. (4a)]. For collinear easy-plane AFM, the coupling is zero in the absence of externally applied magnetic fields. For noncollinear AFMs, ACMPs emerge from the coupling with the dynamics of both the canted net magnetic moment $\left[\propto \sqrt{(2\gamma(H_D+H_0)^2)/\omega_0 H_E}\right]$ and the Néel vector $\left(\propto \sqrt{2\omega_0/\gamma H_E}\right)$, depending on the photon polarization [Eqs. (4b) and (4c)]. Depending on the strength of the Dzyaloshinskii-Moriya interaction (DMI) field, H_D, and on the frequency gap, ω_0, one can employ different strategies to reach the strong-coupling regime.

III. EXPERIMENT

We then turn to an experimental demonstration of antiferromagnetic cavity magnon polaritons using single crystals of hematite (α-Fe_2O_3, initial volume of 12.5 mm^3). We place the sample in a three-dimensional rectangular microwave cavity [Fig. 1(a)] designed with COMSOL® and with cavity resonances from 18 to 45 GHz (see Appendix A). As schematically shown in Fig. 1(a), we record the reflective absorption spectrum of our hybrid system with a vector network analyzer (VNA) while sweeping the external magnetic field, H_0. At T_{Morin}, the magnetic configuration of hematite changes from a noncollinear CEP (induced by a bulk DMI) antiferromagnet to an EA collinear AFM for $T < T_{\text{Morin}}$. Hematite also possesses AFM modes accessible at tens of GHz [Fig. 1(c)]: for $T > T_{\text{Morin}}$, a right-handed low-frequency mode (with a gap of about 15 GHz, due to the small in-plane anisotropy); for $T < T_{\text{Morin}}$, a high-frequency left-handed AFM mode

TABLE I. Summary of the AFM resonance frequencies, $\omega_{0,\pm}$, and coupling strength, $\tilde{g}$, associated with ACMPs for collinear easy-axis ($H < H_{\mathrm{SF}}$, the spin-flop field) and noncollinear canted AFMs. H_E denotes the exchange field. For collinear easy-axis AFMs, $H_{A'}$ stands for the easy-axis anisotropy field and H_0 for the magnetic field applied along the easy axis. For the noncollinear AFMs, H_0 stands for the magnetic field applied along the canted moment. For the canted easy-plane case, H_a stands for the hard-axis anisotropy and $H_{A'}$ is the weak easy-axis anisotropy within the easy plane. In contrast, setting $H_a = 0$ yields a description of canted easy-axis antiferromagnets. Expressions of the coupling strength show that it is independent of the applied magnetic field, H_0, in the collinear easy-axis case and that the coupling strength depends on the magnetic field and on the polarization of the cavity photons in the noncollinear canted case. Subscripts x, y (z) denote the photon mode that propagates in the x direction with an electric field polarized in the y (z) direction. Here, the y axis is the easy axis.

Magnetic ordering	Collinear (easy-axis) AFM($H < H_{\mathrm{SF}}$)	Noncollinear (canted) AFM
Frequencies [34,42]	$\omega_{0,\pm} = \gamma\sqrt{2H_E H_{A'}} \pm \gamma H_0$ (3a)	$\omega_{0,+} = \gamma\sqrt{2H_E(H_{A'} + H_a) + H_D(H_D + H_0)}$ (3b) $\omega_{0,-} = \gamma\sqrt{2H_E H_{A'} + H_0(H_0 + H_D)}$ (3c)
Coupling strength [41]	$\tilde{g}_{\mathrm{EA}} = g'\left(\frac{H_{A'}}{8H_E}\right)^{1/4}$ (4a) with $g' = g_0\sqrt{2NS}$	$\tilde{g}_{x,z,\,\mathrm{CEP}} = -ig'\sqrt{\frac{2\gamma(H_0 + H_D)^2}{\omega_0 H_E}}$ $\tilde{g}_{x,y,\mathrm{CEP}} = g'\sqrt{\frac{2\omega_0}{\gamma H_E}}$ (4b, 4c)

that can be softened to GHz frequencies with an externally applied field (due to a spin-flop field of less than 8 T [43]). The corresponding orientation of the magnetic sublattices for these two modes is shown in Figs. 1(c) and 1(e). This variety of AFM modes renders hematite a well-suited model system for investigating ACMPs in collinear and canted AFMs and to generalize the existence of ACMPs in these two distinct types of AFMs. We choose the polarization of the photon propagation to be perpendicular to the easy axis in the EA phase [Eq. (4a)] and to the canted moment in the CEP phase [Eq. (4b)] to maximize the coupling between the cavity field and the magnons. As expected, the resonance frequency decreases with applied field for the left-handed mode in the collinear EA phase and increases for the right-handed mode in the noncollinear CEP phase. The presence of avoided level crossing (anticrossing) with a frequency gap of $\Delta\omega_{\mathrm{gap}} = 2\tilde{g}$ under resonant coupling conditions ($\omega_c = \omega_m = \omega_0$) represents the hallmark of strongly coupled cavity photon-magnon states, which is the ACMP. As shown in Fig. 1, we observe unambiguous evidence of such anticrossings in both phases exemplarily shown at $T = 100$ K (b) and at $T = 300$ K (d). However, the anticrossings are much clearer and more numerous in the CEP phase. Only the anticrossing at 21 GHz is of similar strength in the two phases due to an external magnetic field that is too low to saturate the sample [43].

IV. ANALYSIS AND DISCUSSION

We determine the coupling strength by fitting the anticrossings for the lowest AFM modes in the EA and CEP phases (cf. Table III in Appendix D). In Figs. 2(a) and 2(b), we display the coupling strength in the two AFM phases. For different cavity modes, the coupling strength reaches hundreds of MHz in the two phases, with larger values in the canted phase. This observation demonstrates that one can stabilize ACMPs through the coupling between cavity photons and the dynamics of both compensated and canted AFMs. For the same cavity modes in the frequency range 37–41 GHz, we observe an enhanced coupling strength by about a factor of 3 in the CEP phase (with values up to 1 GHz in the CEP phase at 300 K and 400 MHz in the EA phase at 100 K).

Using COMSOL® Multiphysics and analytical modeling (see Appendixes A and B), we achieve a quantitative comparison of the experimental and theoretical coupling strengths. We first simulate the cavity mode and extract the simulated mode volumes to determine the single-spin coupling strength ($g_0/2\pi \approx 123$ and 120 mHz for modes at 21 and 37.5 GHz, respectively). Using the values of anisotropy, exchange, and DMI fields in hematite, we obtain theoretical values of $\tilde{g}$ from Eq. (4b) [green and blue dotted lines in Fig. 2(a) and Table II in Appendix D, shaded areas indicate the error bars for the analytical estimation] as a function of temperature. In Fig. 2(a), we notice clear agreement between theory and experiments above and far below the Morin transition. Only near the Morin transition does the coupling strength of the modes around 20 and 40 GHz [see spectra in Fig. 2(b)] collapse further than the theoretical one. This may be associated with both the temperature dependency of the dielectric constant of hematite and the magnon gap around the Morin transition. However, such dependency is out of the scope of our work. Here, the theoretical and experimental temperature dependency of the coupling strength highlights the role of the DMI and

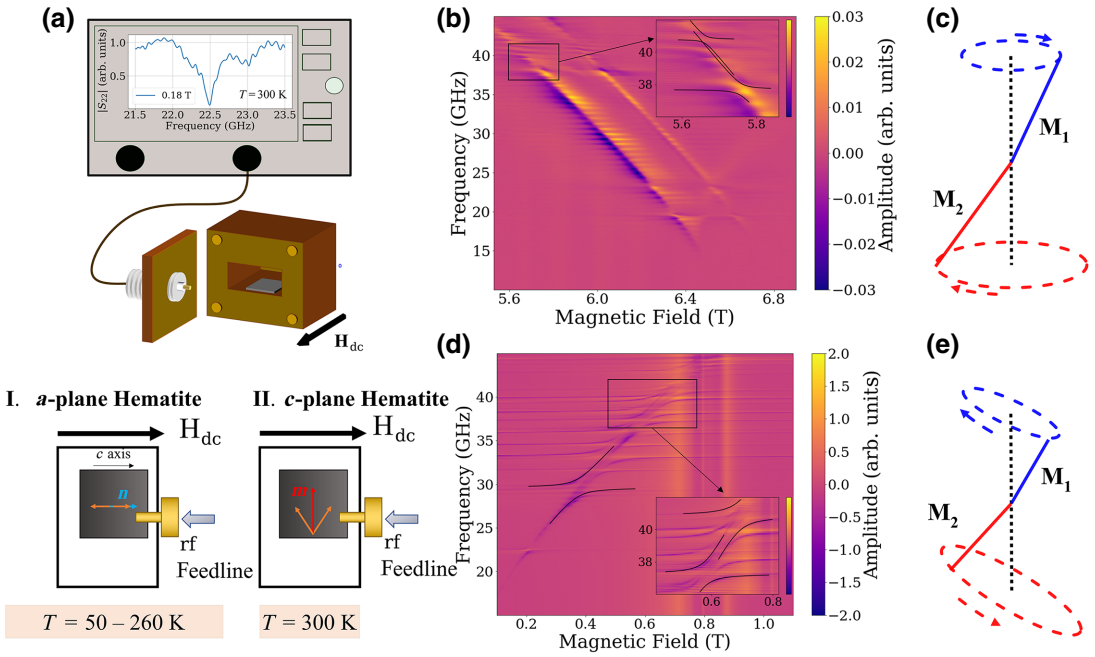

FIG. 1. Cavity photon-magnon polaritons in the collinear and canted phase of hematite. (a) Schematics of the experimental setup employing reflective vector network analysis. Using hematite, we perform temperature-dependent measurements for antiferromagnets with different symmetries, in the easy-axis ($T = 50$–260 K) and canted easy-plane phases ($T = 300$ K). External magnetic field, H_0, is aligned with the easy axis in the collinear phase (*a*-axis sample) and perpendicular to the hard axis (*c*-axis sample) in the easy-plane phase of hematite. "VNA image" shows data for the cavity resonance at 22.5 GHz at 300 K at 180 mT. (b) Exemplary spectrum of the reflection measurement (S_{22}) at $T = 100$ K. Inset shows a magnification of two avoided crossings at higher frequencies, including fits with $\omega_0/2\pi = 37.5$ and 40.8 GHz and $\tilde{g}_{EA}/2\pi = 371$ and 250 MHz, respectively. (c) Sublattice orientation of the left-handed mode of hematite in the easy-axis phase. (d) Reflective-amplitude spectrum of the ACMP in the CEP phase at $T = 300$ K with a fitted anticrossing at 29.5 GHz, with $\tilde{g}_{CEP}/2\pi = 1$ GHz. Inset, magnification and fit at 37.5 GHz with $\tilde{g}_{CEP}/2\pi = 771$ MHz and 40.8 GHz with $\tilde{g}_{CEP}/2\pi \approx 930$ MHz. Comparison of (b),(d) with the fits shows a generic strong enhancement in the CEP phases. (e) Sublattice orientation of the right-handed mode of hematite in the easy-plane phase. Sample size is $5 \times 5 \times 0.5\,\text{mm}^3$ for both phases.

anisotropy fields in, respectively, the canted and collinear phases.

We finally quantify the degree of coherent information exchange between AFM magnons and photons via the cooperativity, $C = \tilde{g}^2/(\kappa_c\kappa_m)$, thus comparing the coupling strength to the photon and magnon dissipations. For this purpose, we also extract the cavity resonator's linewidth [see Fig. 3(a), green squares] for each cavity mode and the magnon linewidth (blue circles) from conventional stripline antiferromagnetic measurements (see Appendix C). As shown in Fig. 3(a), we measure a total decrease of the magnon linewidth from 50 to 300 K in agreement with previous reports [43]. From the values of $\tilde{g}$, κ_c, and κ_m, we then determine the cooperativity of the hybridized states [see Fig. 3(b)].

For $T < 150$ K, we achieve $C > 1$ (green dotted line for $C = 1$), exceeding $C > 4$ at $T = 150$ K. Thus, even in the absence of a net static magnetic moment, the coupling between the Néel-order dynamics and the cavity field is strong enough to enable coherent information transfer. This is the first crucial step for coupling the ACMP to other (nonlinear) systems [17,41]. In the canted phase, we achieve up to $C \approx 70$ (for anticrossing at 29 GHz), which is far above $C = 1$, highlighting the potential of canted AFM for cavity spintronics.

Finally, we determine the coupling strength for different sample volumes from the corresponding anticrossings [2.5 to 12.5 mm^3, see inset in Fig. 3(b)]. As expected, the coupling strength scales with the number of contributing spins originating from the weak canted moment, i.e., the relative spin number, N/N_0, where N_0 is the spin number of the largest sample (black squares, dotted). As expected from Eq. (4), we observe that the coupling strength follows $\tilde{g} \propto \sqrt{N/\omega_0}$. Note that the sample volume induces a frequency shift of the cavity resonance, ω_0 (see Appendix A for more details). As the sample volume, V, scales with N, we predict for the mode with $C \approx 70$ at 29 GHz a cooperativity of $C > 1$, even with hematite spheres as small as about 0.7 mm in diameter. The prevailing existence of ACMPs for different sample sizes represents another key feature to open future research directions in cavity magnonics, such as further downscaling. As concluding

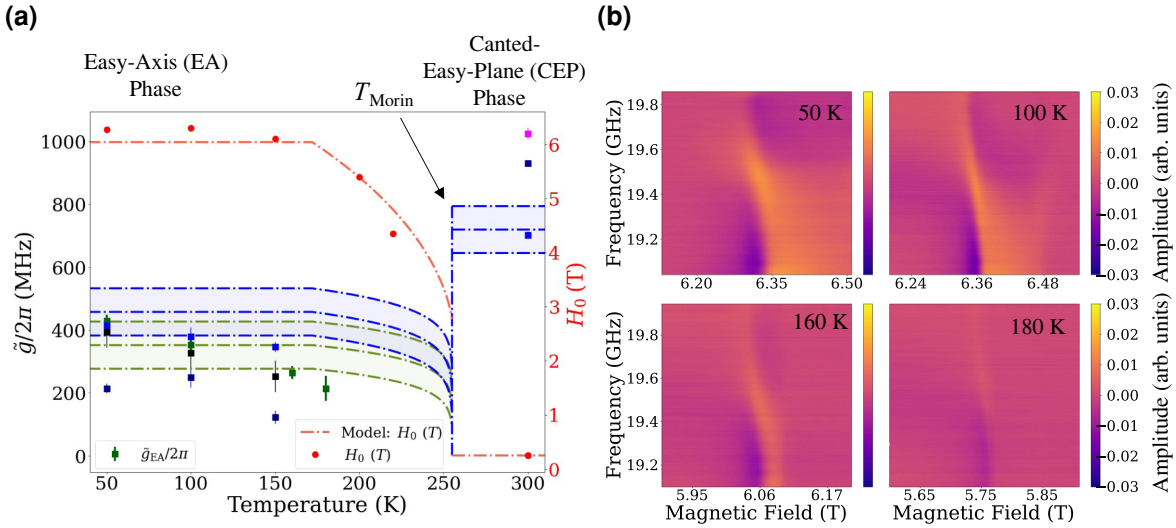

FIG. 2. Effective coupling strength of ACMPs. (a) Resonant fields (red circles) and experimental values for $\tilde{g}(T)$ across the Morin transition for different modes [dark blue, 40.8 GHz; black (green), 20.8 GHz (19.5 GHz); magenta, 29 GHz; and blue, 37.5 GHz]. Expectations based on our theoretical model are shown as dashed lines. Datasets around 21 GHz are two independent datasets measured for the same cavity-resonator mode. Notably, resonance frequencies shifted due to changes in the sample position between both measurements (Appendix D) towards the Morin transition ($T \sim 260$ K); coupling strength decreases due to the decreasing easy-axis anisotropy field, $H_{A'}$ (red circles, extracted $H_{A'}$ from resonance frequencies). Correspondingly, for $T > T_{\mathrm{Morin}}$, coupling strength agrees with the theoretical value within error bars, exemplarily shown for 37.5 GHz [cf. Eq. (4)]. (b) Anticrossing spectra at different temperatures for a resonance frequency of 19.5 GHz, showing collapse of the coupling strength in the collinear phase, towards the phase transition at T_{Morin}. VNA output power level is set to -6 dBm.

remarks, we first want to emphasize that the theoretical coupling strength of a $5 \times 5 \times 0.5$-mm^3 sample of hematite in the CEP phase yields (202 ± 4) MHz at 21 GHz, which is similar to a ferromagnetic YIG sphere with a diameter of 1 mm, (263 ± 11) MHz, i.e., with about 1/24 of the AFM volume (see Table III in Appendix D for experimental

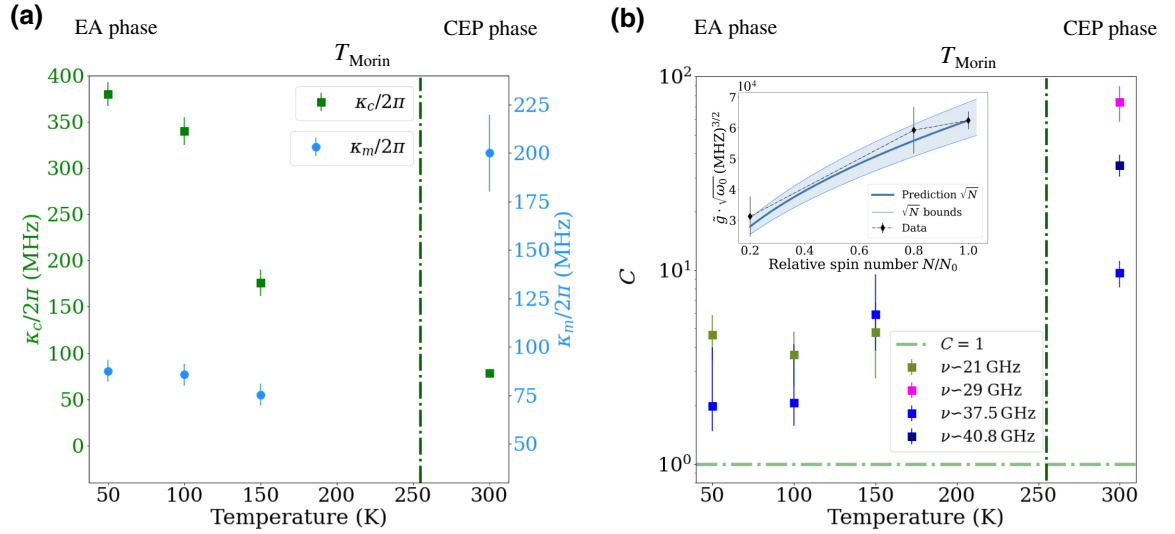

FIG. 3. Coherence of the magnon-photon (hybrid states). (a) Temperature dependence of the cavity resonator's (green) and magnon linewidth (blue). Magnon linewidth decreases towards T_{Morin}, in line with previous observations [43]. (b) Temperature dependence of cooperativity, C, in the collinear easy-axis phase and the canted easy-plane phase of hematite. $C > 1$ is observed at all temperatures, indicating a coherent exchange of information. Anticrossings at larger frequencies for selected modes [21 (green), 29 (magenta), 37.5 (blue), and 40.8 GHz (dark blue)] in the CEP phase show much larger cooperativities [e.g., $C = (73 \pm 16)$ for the mode at 29 GHz]. Inset, coupling-strength dependency for three different sample sizes at 300 K. Experimental coupling strengths (black dotted line) agree with the theoretical prediction using upper and lower bounds. For size-dependent data, the VNA output power level is set to -17 dBm.

confirmation). Second, some orthoferrites [44–49] can have much larger DMI fields than hematite, and sub-THz resonance frequencies can generate ACMPs for a smaller sample size and different symmetry of photon polarizations (Table I).

V. SUMMARY

We demonstrate the strong-coupling regime between a microwave cavity field and collective spin excitations in both collinear and noncollinear antiferromagnets over a wide temperature range. Theoretically and experimentally, we highlight that the coupling strength scales with the material's anisotropy, exchange, and DMI fields. Altogether, despite the small or vanishing net moments, our results highlight the potential of using insulating antiferromagnets with different magnetic symmetries for cavity spintronics with enhanced control of the magnon-photon polaritons. We would also like to point out that, despite a larger linewidth (due to the large exchange field), we can reach the strong-coupling regime with antiferromagnetic CMPs. This is further quantified by obtaining a cooperativity of $C > 1$. Our observations enable the road to hitherto unexplored ranges of physics and provide further insight into light-matter interactions and nonlinear information-processing devices benefiting from the rich variety of different symmetries of antiferromagnets [50]. Finally, the prospects of much higher accessible resonance frequencies for antiferromagnetic cavity spintronics open the way to integrating ACMPs into spintronic and magnonic devices.

ACKNOWLEDGMENTS

I.B. and R.L acknowledge support from the French Agence Nationale de la Recherche (ANR) under grant ANR-22-CE24-0008-03 (ICARUS). R.L., I. B., A.A. and M.K. acknowledge financial support from the Horizon 2020 Framework Programme of the European Commission under FET-Open grant agreement no. 863155 (s-Nebula). I. B. and R. L. acknowledges financial support from the Horizon 2020 Framework Programme of the European Commission under FET-Open grant agreement No. 964931 (TSAR). M.K. acknowledges support from the Graduate School of Excellence Materials Science in Mainz (MAINZ) DFG 266, the DAAD (Spintronics network, Project No. 57334897). M.K. acknowledges support from the DFG project number 423441604 and 268565370 (f Project A01). The Research Council of Norway supported H.T.S., B.B, M.K., and A.B. through its Centers of Excellence funding scheme, project number 262633 "QuSpin".

APPENDIX A: EXPERIMENTAL SETUP(S)

1. CAVITY MEASUREMENTS

The temperature-dependent measurements from 50 to 300 K are performed by employing a physical property measurement system (PPMS) from Quantum Design with maximal magnetic fields of up to 9 T. Another setup at room temperature is comprised of a standard room-temperature ferromagnetic resonance setup with fields up to 1.5 T. For the number dependence of the coupling strength [cf. inset in Fig. 3(b)], we employ this setup, as illustrated in Fig. 4(c). For both experimental setups, data acquisition is conducted by means of vector network analysis by utilizing a PNA E8364C vector network analyzer up to 50 GHz. The VNA output power level for the measurements at 300 K with the setup shown in Fig. 4(c) is set to −17 dBm and for the measurements in the PPMS to −6 dBm. Typically, a short-open-load-through (SOLT) calibration is performed before the (low-temperature) measurements by using an Agilent N4693-60001 electronic calibration module to reduce the contribution of a field-independent constant background to the measured spectra and enhance the signal-to-noise ratio.

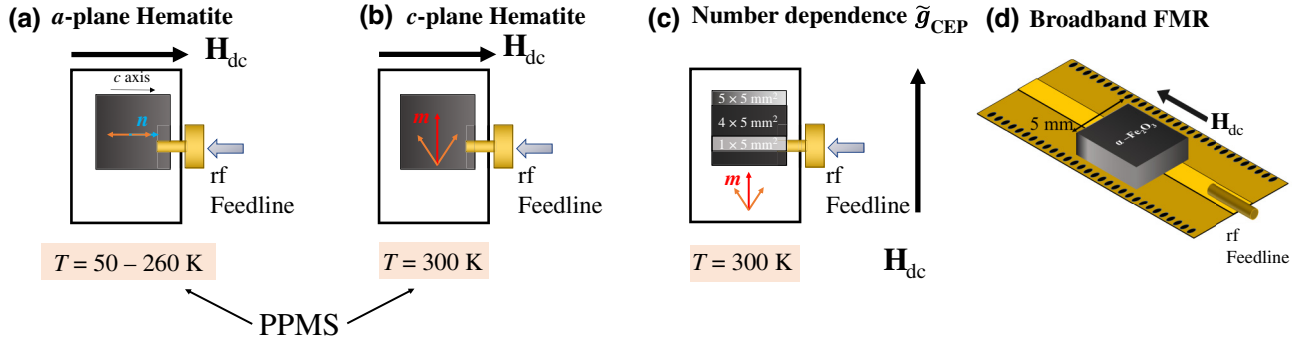

FIG. 4. Schematics of the two experimental setups employed to investigate cavity magnon polaritons in α-Fe_2O_3. (a) For cryogenic measurements in the easy-axis phase, we use a PPMS from Quantum design, where the dc magnetic field is along the short cavity axis and an a-plane-cut hematite crystal (size, $5 \times 5 \times 0.5$ mm^3). (b) At 300 K, we use a c-plane-cut hematite crystal of the same dimensions. (c) Schematics of the experimental setup employed for the number dependence of the coupling strength in the easy-plane phase [(cf. inset in Fig. 3(b)]. (d) Schematics of the experimental setup for the broadband ferromagnetic resonance (FMR) experiments.

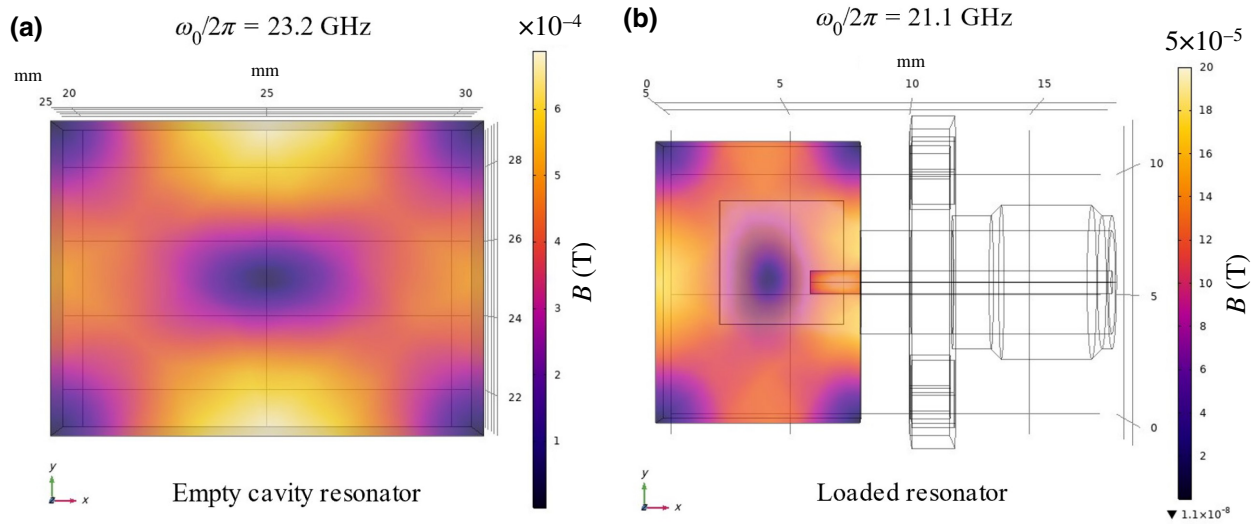

FIG. 5. COMSOL® simulation of the cavity mode with the lowest resonance mode. Top view of the cavity resonator and capacitive coupling into the resonator for (a) the empty-cavity resonator and (b) the loaded-cavity resonator with a $5 \times 5 \times 0.5$-mm^3 sample. Notably, resonance frequencies for the same resonance mode distribution in the cavity resonator differ by 2 GHz due to insertion of the dielectric by means of the sample and the coupling pin. Distance of the sample for the simulations with no parametric position sweep in the x direction to the right border of the cavity volume is set to 0.7 mm.

II. BROADBAND FMR

To determine the magnon dissipation parameter, κ_m, we record both the cavity photon-magnon polariton spectra far from any cavity resonance and the stripline ferromagnetic resonance. For this second approach, we perform derivative stripline FMR using a broadband coplanar waveguide, specifically lock-in detection with a Stanford Research Systems SR860 lock-in amplifier and the same electromagnet as that used for CMP measurements with a modulating coil [cf. Fig. 1(d)].

III. DESIGN OF THE CAVITY

The resonance frequencies of antiferromagnets are typically much higher than those of comparable ferro- (ferri-) magnets. Therefore, resonant coupling between antiferromagnetic resonance modes requires designing cavity resonators with higher cavity-resonance frequencies. We utilize a comparably small (relative to conventional CMP setups) rectangular cavity resonator made of copper (height × width × depth = $4.5 \times 11 \times 8$ mm^3). The cavity resonator is designed for microwave reflection measurements. Specifically, the cavity is equipped with one input port. The cavity's standing-wave modes are excited by the capacitive coupling of the microwave input to the mode's electric field (cf. Fig. 5). In addition, we place the samples slightly off the cavity center to address more antinodes of the cavity field and optimize the coupling efficiency, as illustrated in the image from the COMSOL® simulation in Fig. 5(a) for the first cavity mode with the lowest frequency.

IV. IDENTIFICATION OF THE CAVITY MODES ASSOCIATED WITH CMPS

A. Identification of the cavity-resonator modes

In experimental data, we observe several anticrossings in a frequency window of 18–45 GHz. To compare theory and experiments and perform a comparison of the CMP in the EA and CEP phases, as shown in Figs. 1–3, one needs to identify with precision the cavity-resonator modes.

For our measurements, we utilize an a-plane- (c-plane-) oriented $5 \times 5 \times 0.5$-mm^3 bulk hematite crystal for measurements in the easy-axis phase for $T < T_{\mathrm{Morin}}$ ($T = 300$ K). To also investigate the size (spin number) dependence of the coupling strength in the CEP phase, we also measure with a set of differently sized c-plane-oriented samples. The sample dimensions are (w, width; l, length; t, thickness): (I) $w = 1$, $l = 5$ mm, $t = 0.5$ mm; (II) $w = 3$, $l = 5$ mm, $t = 0.5$ mm; (III) $w = 4$ mm, $l = 5$ mm, $t = 0.5$ mm; and (IV) $w = 5$ mm, $l = 5$ mm, $t = 0.5$ mm. Please note that we use a room-temperature-only setup, where the static field is perpendicular to the c-axis orientation for the number dependence only.

For small sample volumes, the fractional decrease in the resonance frequency of the cavity modes can be approximated to [51]

$$\frac{\omega - \omega_0}{\omega_0} = -\frac{\int_{V'_0}(\Delta\epsilon|E_0|^2 + \Delta\mu|H_0|^2)dV'}{\int_{V_0}(\epsilon|E_0|^2 + \mu|H_0|^2)dV}. \tag{A1}$$

The resonance frequencies of the loaded-cavity modes then differ significantly from the empty-cavity resonances. For a magnetic sample with dimensions $x = a'$ (width),

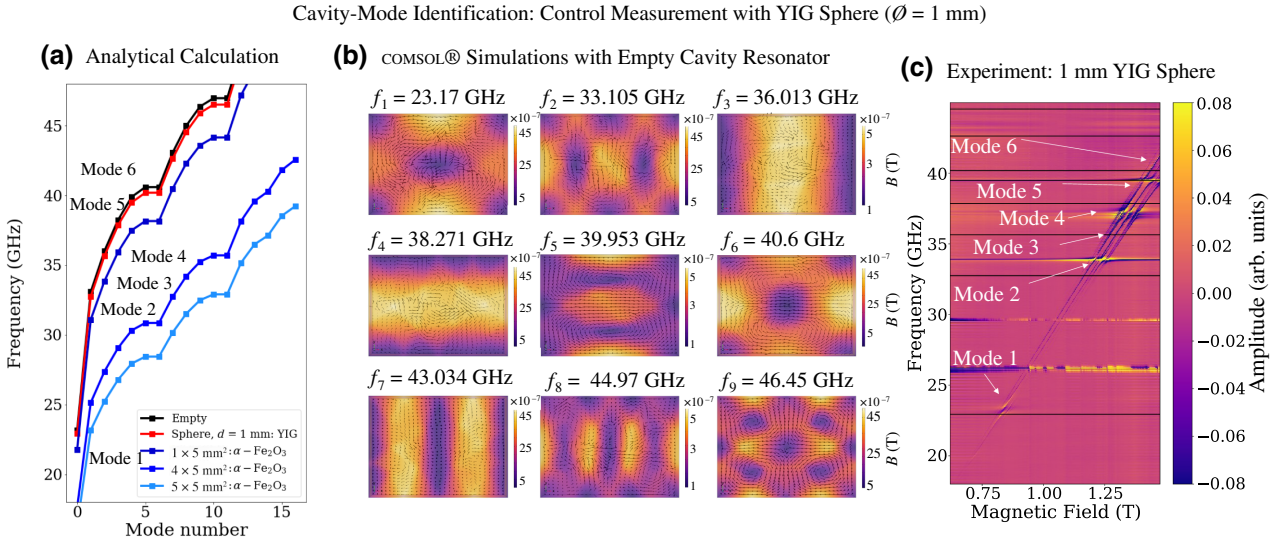

FIG. 6. Identification of cavity-resonator modes. (a) Calculated resonance-frequency shift for the insertion of different sample sizes used in our experiments, including reference measurements using a millimeter-sized YIG sphere ($\varnothing = 1$ mm). (b) Result of an empty-cavity COMSOL® simulation showing the resonance frequency and respective magnetic-ac-field mode distribution. (c) Comparison of the experimentally obtained cavity-resonance anticrossings for a YIG sphere placed in the center of the cavity resonator with the resonance frequencies, as calculated from the shift and simulation (horizontal black lines).

$y = d'$ (depth), and $z = t'$ (height), the corresponding frequency change for the loaded-cavity resonator can be calculated via

$$\frac{\omega - \omega_0}{\omega_0} = -(\epsilon_r - 1)\frac{a't'd'}{2abd}, \tag{A2}$$

where ω denotes the shifted resonance frequency of the cavity-resonator mode; ω_0 is the unperturbed cavity-resonance frequency; ϵ_r is the (real part of the) dielectric constant of the inserted magnetic sample; and a, b, and d are the cavity-resonator dimensions. The largest hematite samples we use (5 mm wide, 5 mm long, and 0.5 mm high) have a volume corresponding to 3.16% of the cavity volume. Thus, for the dielectric constant of hematite, $\epsilon_r = 19.1$ [36], the presence of the sample can

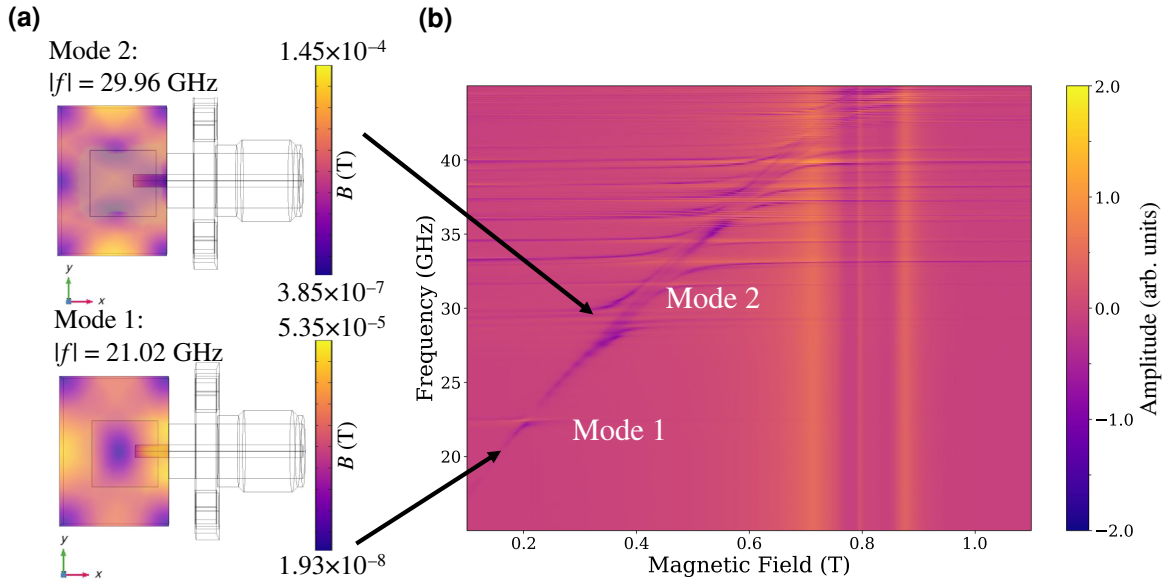

FIG. 7. Mode identification for a $5 \times 5 \times 0.5$-mm^3 sample based on COMSOL® simulations. (a) Mode distribution for 21 and 29 GHz. (b) Spectrum at 300 K. Modes around 21 and 29.9 GHz are highlighted by black arrows and identified as the same modes 1 and 2 for the YIG sample. Small frequency shift between theory and experiments can be assigned to the small difference in sample positions [see Appendix D III].

shift the resonance frequencies of the cavity modes by a few GHz, as outlined in Fig. 6(a). This adds complexity to the identification of the cavity modes in experiments and comparison with COMSOL® simulations that can provide the mode profiles.

To benchmark our approach to identify the cavity modes, we thus first compare the COMSOL® simulations of an empty cavity with cavity measurements performed with a small YIG sphere ($\varnothing = 1$ mm) purchased from Ferrisphere Inc.® The volume of the YIG sphere is much smaller than the mode volume of the resonator, and thus, modifies the cavity-resonator modes only weakly, resulting in slight lowering of their resonance frequencies. Thus, a YIG sphere is a good probe to characterize the experimental cavity modes and compare them with simulations and analytical calculations. We can then associate in Fig. 6 the mode simulated in COMSOL® (b) with the experimental results of a YIG sphere (c) with the frequency shift obtained for each mode with Eq. (A2). In Fig. 6(b), we calculate the corresponding shift with the analytical formula as well [Fig. 6(a)]. As shown in Fig. 6(c), the comparison with experimental data shows excellent agreement with measurements.

We can then apply Eq. (A2) to identify the frequency shift expected for each mode in the presence of hematite samples, and we also perform COMSOL® simulations in a presence of a large dielectric piece [similar to the hematite sample, see sketch in Fig. 7(a)]. Similarly to Fig. 6(c), we then obtain [Figs. 7(a) and 7(b)] the correspondence between the analytical resonance frequencies [Fig. 6(a)], the COMSOL® simulations, and the measurements at room temperature for a $5 \times 5 \times 0.5$-mm^3 hematite sample.

V. CRITERIA FOR CAVITY-RESONATOR MODES ACHIEVING ACMP

One must notice that, in principle, all the present cavity modes can couple with FM and AFM magnons. However,

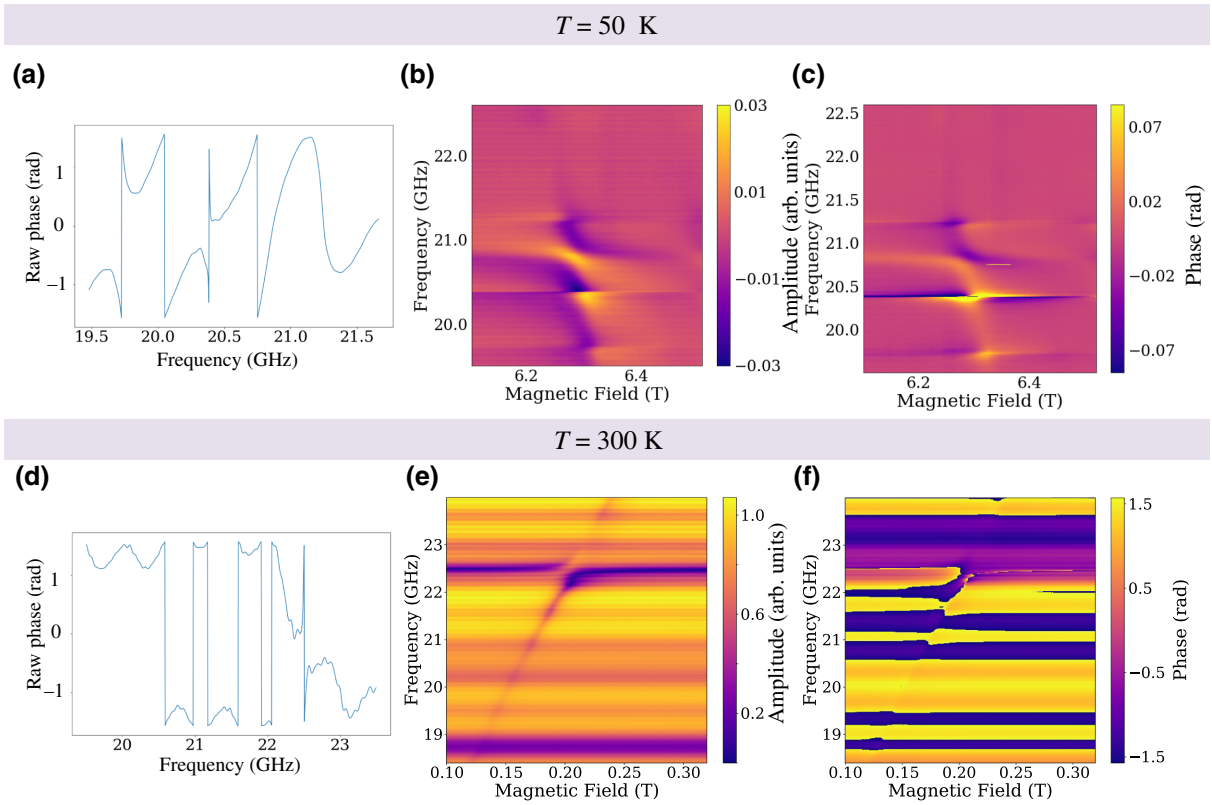

FIG. 8. Identification of strong coupling for the mode at 20.8 GHz. (a) Magnification of raw (unprocessed) phase data for the spectrum shown in Fig. 1(b) and the corresponding inset. Resonance at 20.8 GHz and additional resonances at 19.73, 20.36, and 21.21 GHz are displayed. For modes at 21.21 and 20.36 GHz, the phase jump is smaller than π, indicating dominating external losses (from microwave feedline losses), and hence, weakly coupled cavity modes. Resonance at 19.73 GHz does not couple coherently [cf. (b)]. (b),(c) Observation of additional anticrossings apart from the discussed anticrossing at 20.8 GHz for hematite in the collinear phase, here exemplarily shown for $T = 50$ K. (b) Background-subtracted amplitude and (c) phase representation. Notably, couplings except for that at 20.8 GHz do not correspond to a conservative coupling regime (@ 19.73 GHz) or are not in the strongly coupled regime (@20.36 and 21.21 GHz). (d)–(f) Same representation for the equivalent mode in the CEP phase at 300 K, showing the raw data spectrum. One can clearly see only one anticrossing at 22.5 GHz, which corresponds to mode 1. Other horizontal lines in (e) are from the field-independent background and, accordingly, the picked-up phases (f).

not all of them lead to a strong-coupling regime. There are two key features that define the possibility of stabilizing the ACMP for a given cavity mode.

First, weakly coupled (evanescent waveguide) modes also do not couple efficiently with magnons. As shown in Fig. 8 for an exemplary spectrum taken at 50 K for the dataset with a resonance at 20.8 GHz, there are various cavity modes (at 19.73, 20.36, and 21.21 GHz) around the mode at 20.8 GHz. However, only the one at 20.8 GHz leads to an anticrossing. The phase response of our $|S_{22}|$ spectra enables us to identify the cavity modes of interest to observe the ACMP. Furthermore, in the COMSOL® simulations, one can identify these modes by their large imaginary part in the obtained resonance frequency. The insertion of a comparably large sample with a high dielectric constant results in cavity resonances where the dielectric losses dominate over the coupling losses to the feedline (over the coupled cavity resonator). In the spectrum, this condition is represented by a jump in the phase by $\geq \pi$ at the resonance frequency of the cavity mode. As one can infer from Fig. 8(a), the modes at 20.36 and 21.21 GHz exhibit a phase jump smaller than π, indicating weakly coupled cavity modes. Lastly, the mode at 19.73 GHz also exhibits a phase jump of π. However, the shape of each branch in the vicinity of $\omega_c = \omega_m = \omega_r$ appears to correspond to the dissipative coupling regime rather than the conservative one. Contrary to the slope of the upper and lower branches for an anticrossing, the slope of the hybridized state approaching resonant coupling seems to be "attracted." This is opposite to the case of the anticrossing. Although interesting, this is a subject for another study and out of the scope of this work. Thus, in this frequency range, only the cavity mode at 20.8 GHz possesses the key features to lead to an ACMP. For all measurements, we perform a SOLT calibration at room temperature, which becomes less accurate towards lower temperatures. Hence, please note that the remaining visible phase jump at 20.0 GHz is an additional phase picked up from the rf background in the reflection VNA measurement and does not correspond to any resonance.

Second, the symmetry between the dc and ac magnetic fields does not always enable an efficient coupling between the cavity photons and the magnons. The exciting ac magnetic field must be orthogonal to the Néel vector to excite the low-frequency mode in the easy-axis phase and transverse to the canted moment to excite the low-frequency mode in the canted phase. In the main text [see sketch in Fig. 1(a) and Appendix A I], we use an *a*-plane sample below the Morin transition and a *c*-plane sample above the Morin transition, so that the canted moment and the Néel vector have the same direction when applying an external magnetic field, which allows us to make a direct comparison between the easy-axis and canted easy-plane phases.

APPENDIX B: DERIVATION OF THE EFFECTIVE COUPLING CONSTANT

In this section, we derive the effective coupling constant relating canted antiferromagnets and cavity photons. That is, we consider the third term of the phenomenological Hamiltonian:

$$\mathcal{H}_{\text{sys}} = \mathcal{H}_c + \mathcal{H}_{\text{AFM}} + \mathcal{H}_{\text{CAFM}} \ , \tag{B1}$$

where as the first two terms correspond to the cavity modes and the antiferromagnetic magnon modes, respectively. As a starting point, we derive the magnon eigenmodes of the antiferromagnet. Then we consider the photon modes and the coupling that gives rise to the magnon polariton.

I. ANTIFERROMAGNETIC MAGNONS IN CANTED ANTIFERROMAGNETS

The antiferromagnet is described by the Hamiltonian

$$\mathcal{H}_{\text{afm}} = J \sum_{\langle i,j \rangle} \mathbf{S}_i \cdot \mathbf{S}_j + |\gamma| \sum_i H_0 S_i^x + \frac{K_z}{2} \sum_i (S_i^z)^2 - \frac{K_y}{2} \sum_i (S_i^y)^2 + D \sum_{\langle i,j \rangle} [\mathbf{S}_i \times \mathbf{S}_j]_z. \tag{B2}$$

Here, J is the exchange interaction, H_0 is a constant applied magnetic field, and D is the DMI constant. In the case of a canted easy-plane antiferromagnet, K_z quantifies the strong hard-axis anisotropy and K_y the weak easy-axis anisotropy. In contrast, the limit $K_z = 0$ yields a description of canted easy-axis antiferromagnets. The subscripts i and j of the spin operators $\mathbf{S}$ are the lattice sites, whereas $\langle i,j \rangle$ denotes nearest-neighbor sites. The DMI and external magnetic field give rise to a small canting angle, $\pi/2 - \theta \lessapprox \pi/2$.

To consider the canting angle, we introduce two coordinate systems: $\{x', y', z'\}$ and $\{x'', y'', z''\}$. Let the principal axis of each sublattice coincide with the axes $\hat{\mathbf{x}}'$ and $\hat{\mathbf{x}}''$, respectively. Furthermore, let the $\hat{\mathbf{z}}$ axes coincide with the crystal $\hat{\mathbf{z}}$ axis such that $\hat{\mathbf{z}}' = \hat{\mathbf{z}}'' = \hat{\mathbf{z}}$. Lastly, we let $\hat{\mathbf{y}}' = \hat{\mathbf{z}}' \times \hat{\mathbf{x}}'$ and $\hat{\mathbf{y}}'' = \hat{\mathbf{z}}'' \times \hat{\mathbf{x}}''$. Subsequently, we perform a Holstein-Primakoff transformation to quadratic order in magnon operators:

$$\begin{aligned}
S_i^{x'} &= \hbar(S - a_i^\dagger a_i), \quad S_i^{y'} = \hbar\sqrt{\frac{S}{2}}(a_i + a_i^\dagger), \\
S_i^{z'} &= i\hbar\sqrt{\frac{S}{2}}(a_i^\dagger - a_i), \\
S_j^{x''} &= \hbar(S - b_j^\dagger b_j), \quad S_j^{y''} = \hbar\sqrt{\frac{S}{2}}(b_j + b_j^\dagger), \\
S_j^{z''} &= i\hbar\sqrt{\frac{S}{2}}(b_j^\dagger - b_j).
\end{aligned} \tag{B3}$$

Here, $\hbar$ and S are the reduced Planck constant and the electron spin, 1/2. The magnon annihilation (creation) operators, $a_i^{(\dagger)}$ and $b_j^{(\dagger)}$, act on distinct sublattices. In the following, we consider only macrospin excitations, that is, magnons with quasi-momentum $k = 0$. Hence, we drop the i and j subscripts.

To diagonalize the Hamiltonian, we write it in matrix form with respect to the basis $\boldsymbol{\phi}$. In this form, it is

$$\mathcal{H}_m = \boldsymbol{\phi}^\dagger \mathbf{H} \boldsymbol{\phi}, \tag{B4}$$

with $\boldsymbol{\phi} = [a, a^\dagger, b, b^\dagger]^T$ and

$$H = \gamma\hbar S \begin{pmatrix} -H_E c_2 + H_D s_2 + H_0 c + H_{A'}\left(s^2 - \frac{c^2}{2}\right) + \frac{H_a}{2} & -\frac{H_a + H_{A'} c^2}{2} & \frac{H_E(c_2+1) - H_D s_2}{2} & \frac{H_E(c_2-1) - H_D s_2}{2} \\ -\frac{H_a + H_{A'} c^2}{2} & -H_E c_2 + H_D s_2 + H_0 c + H_{A'}\left(s^2 - \frac{c^2}{2}\right) + \frac{H_a}{2} & \frac{H_E(c_2-1) - H_D s_2}{2} & \frac{H_E(c_2+1) - H_D s_2}{2} \\ \frac{H_E(c_2+1) - H_D s_2}{2} & \frac{H_E(c_2-1) - H_D s_2}{2} & -H_E c_2 + H_D s_2 + H_0 c + H_{A'}\left(s^2 - \frac{c^2}{2}\right) + \frac{H_a}{2} & -\frac{H_a + H_{A'} c^2}{2} \\ \frac{H_E(c_2-1) - H_D s_2}{2} & \frac{H_E(c_2+1) - H_D s_2}{2} & -\frac{H_a + H_{A'} c^2}{2} & -H_E c_2 + H_D s_2 + H_0 c + H_{A'}\left(s^2 - \frac{c^2}{2}\right) + \frac{H_a}{2} \end{pmatrix}, \tag{B5}$$

with the shorthand notation $s = \sin\theta$, $c = \cos\theta$, $s_2 = \sin 2\theta$, and $c_2 = \cos 2\theta$. In this form, all constants are in terms of fields. They are defined as $H_E = Jz/\gamma$, $H_D = Dz/\gamma$, $H_a = K_z/\gamma$, and $H_{A'} = K_y/\gamma$, where z denotes the number of nearest-neighbor sites. For a small easy-axis anisotropy, $H_{A'}$, and $(H_0 + H_D/2H_E) \ll 1$, the equilibrium canting angle is $\theta \approx \arccos(H_0 + H_D/2H_E)$. We diagonalize the Hamiltonian through a generalized Bogoliubov transformation, as done in Ref. [52].

The properly normalized transformation matrices are

$$\begin{pmatrix} a \\ a^\dagger \\ b \\ b^\dagger \end{pmatrix} = \gamma\hbar S \begin{pmatrix} u_\alpha & v_\alpha & -u_\beta & v_\beta \\ v_\alpha & u_\alpha & v_\beta & -u_\beta \\ u_\alpha & v_\alpha & u_\beta & -v_\beta \\ v_\alpha & u_\alpha & -v_\beta & u_\beta \end{pmatrix} \begin{pmatrix} \alpha \\ \alpha^\dagger \\ \beta \\ \beta^\dagger \end{pmatrix},$$
$$\begin{pmatrix} \alpha \\ \alpha^\dagger \\ \beta \\ \beta^\dagger \end{pmatrix} = \gamma\hbar S \begin{pmatrix} u_\alpha & -v_\alpha & u_\alpha & -v_\alpha \\ -v_\alpha & u_\alpha & -v_\alpha & u_\alpha \\ -u_\beta & -v_\beta & u_\beta & v_\beta \\ -v_\beta & -u_\beta & v_\beta & u_\beta \end{pmatrix} \begin{pmatrix} a \\ a^\dagger \\ b \\ b^\dagger \end{pmatrix}, \tag{B6}$$

where

$$u_\alpha = \frac{\omega_\alpha + \gamma H_E}{\sqrt{2\omega_\alpha}\sqrt{\omega_\alpha + 2\gamma H_E}}, u_\beta = \frac{\omega_\beta + \gamma H_E}{\sqrt{2\omega_\beta}\sqrt{\omega_\beta + 2\gamma H_E}},$$
$$v_\alpha = \frac{\gamma H_E}{\sqrt{2\omega_\alpha}\sqrt{\omega_\alpha + 2\gamma H_E}}, v_\beta = \frac{\gamma H_E}{\sqrt{2\omega_\beta}\sqrt{\omega_\beta + 2\gamma H_E}}. \tag{B7}$$

Here, $\omega_\alpha = \gamma\sqrt{H_0(H_0 + H_D) + 2H_E H_{A'}}$ and $\omega_\beta = \gamma\sqrt{H_D(H_0 + H_D) + 2H_E(H_a + H_{A'})}$ are the resonance frequencies. In this notation, ω_α is the low-frequency mode and ω_β is the high-frequency mode. The eigenmodes and transformation matrix are derived under the assumption that $H_E \gg H_D \gg H_0$.

II. MAGNON POLARITONS IN CANTED AFMS

In the following, we consider the magnetization and effects of an ac magnetic field to first order in magnon and photon operators. Furthermore, we consider the Zeeman coupling between magnons and photons. This coupling gives rise to the magnon polariton.

The magnetization to linear order in sublattice magnon operators is

$$\begin{aligned} \mathbf{m}^{(1)} = \sqrt{\frac{NS}{2}}\{&\hat{\mathbf{x}} \sin\theta[-(a + a^\dagger) + (b + b^\dagger)] \\ &+ \hat{\mathbf{y}} \cos\theta[(a + a^\dagger) + (b + b^\dagger)] \\ &+ i\hat{\mathbf{z}}[(a^\dagger - a) + (b^\dagger - b)]\}, \end{aligned} \tag{B8}$$

where N is the number of lattice sites in each sublattice. We rewrite the magnetization in terms of the magnon eigenmodes. Transforming to eigenmode operators, we find

$$-(a + a^\dagger) + (b + b^\dagger) = 2(u_\beta - v_\beta)[\beta + \beta^\dagger], \tag{B9}$$
$$(a + a^\dagger) + (b + b^\dagger) = 2(u_\alpha + v_\alpha)[\alpha + \alpha^\dagger], \tag{B10}$$
$$(a^\dagger - a) + (b^\dagger - b) = 2(v_\alpha - u_\alpha)[\alpha - \alpha^\dagger]. \tag{B11}$$

From these eigenmodes, we see that the $\hat{\mathbf{x}}$ component of magnetization $\mathbf{m}^{(1)}$ scales linearly with the high-frequency mode. Conversely, the $\hat{\mathbf{y}}$ and $\hat{\mathbf{z}}$ components scale linearly with the low-frequency mode. We insert the Bogoliubov coefficients, and use $\gamma J \gg \omega_{\alpha/\beta}$. That procedure yields

$$-(a+a^\dagger)+(b+b^\dagger)=\sqrt{\frac{\omega_\beta}{\gamma H_E}}[\beta+\beta^\dagger], \tag{B12}$$

$$(a+a^\dagger)+(b+b^\dagger)=2\sqrt{\frac{\gamma H_E}{\omega_\alpha}}[\alpha+\alpha^\dagger], \tag{B13}$$

$$(a^\dagger-a)+(b^\dagger-b)=\sqrt{\frac{\omega_\alpha}{\gamma H_E}}[\alpha-\alpha^\dagger]. \tag{B14}$$

By linearizing in the canting angle, $\sin\theta \approx 1$ and $\cos\theta = H_0 + H_D/2H_E$, we find the magnetization:

$$\mathbf{m}^{(1)}=\sqrt{\frac{NS}{2}}\left\{\hat{\mathbf{x}}\sqrt{\frac{\omega_\beta}{\gamma J}}[\beta+\beta^\dagger]+\hat{\mathbf{y}}\frac{2(H_0+H_D)}{2H_E}\sqrt{\frac{\gamma J}{\omega_\alpha}}[\alpha+\alpha^\dagger]+i\hat{\mathbf{z}}\sqrt{\frac{\omega_\alpha}{\gamma H_E}}[\alpha-\alpha^\dagger]\right\}. \tag{B15}$$

The magnetization couples to the ac magnetic field through the Zeeman interaction, $\mathbf{m}^{(1)}\cdot\mathbf{B}^{(1)}$. We quantize the external magnetic field to first order in photons:

$$\mathbf{B}_p^{(1)}=\sum_{\mathbf{k}\lambda}\sqrt{\frac{\hbar\omega_{\mathbf{k}\lambda}\mu_0}{V}}\cos\left(\frac{n\pi(\mathbf{k}\cdot\mathbf{r})}{L_{\hat{\mathbf{k}}\cdot\hat{\mathbf{r}}}}\right)[(\hat{\mathbf{k}}\times\mathbf{e}_{\mathbf{k}\lambda})p_{\mathbf{k}\lambda}-(\hat{\mathbf{k}}\times\mathbf{e}^*_{\mathbf{k}\lambda})p^\dagger_{\mathbf{k}\lambda}], \tag{B16}$$

where $p^{(\dagger)}_{\mathbf{k}\lambda}$ denotes the photon annihilation (creation) operator of a photon of momentum $\mathbf{k}$ and polarization λ, and $L_{\mathbf{k}\cdot\mathbf{r}}$ is the length of the cavity in the $\hat{\mathbf{k}}$ direction. The integer n denotes the energy mode of the photon operator with an associated energy $\hbar\omega_{\mathbf{k}\lambda}$. The magnon-photon coupling to quadratic order is then

$$\begin{aligned}\mathcal{H}_{\mathrm{CAFM}}=-i\gamma\hbar\sqrt{\frac{NS\hbar\mu_0}{2V}}\sum_n\Bigg\{&\left[\sqrt{\omega_{n,y}}\cos\left(\frac{n\pi y}{L_y}\right)(p_{n,y,z}-p^\dagger_{n,y,z})-\sqrt{\omega_{n,z}}\cos\left(\frac{n\pi z}{L_z}\right)(p_{n,z,y}-p^\dagger_{n,z,y})\right]\sqrt{\frac{\omega_\beta}{\gamma H_E}}[\beta+\beta^\dagger]\\&+\left[\sqrt{\omega_{n,z}}\cos\left(\frac{n\pi z}{L_z}\right)(p_{n,z,x}-p^\dagger_{n,z,x})-\sqrt{\omega_{n,z}}\cos\left(\frac{n\pi x}{L_x}\right)(p_{n,x,z}-p^\dagger_{n,x,z})\right]2\left(\frac{H_0+H_D}{2H_E}\right)\sqrt{\frac{\gamma H_E}{\omega_\alpha}}[\alpha+\alpha^\dagger]\\&+\left[\sqrt{\omega_{n,x}}\cos\left(\frac{n\pi x}{L_x}\right)(p_{n,x,y}-p^\dagger_{n,x,y})-\sqrt{\omega_{n,y}}\cos\left(\frac{n\pi y}{L_y}\right)(p_{n,y,x}-p^\dagger_{n,y,x})\right]i\sqrt{\frac{\omega_\alpha}{\gamma H_E}}[\alpha-\alpha^\dagger]\Bigg\}.\end{aligned} \tag{B17}$$

In the following, we consider only photons propagating in the $\hat{\mathbf{x}}$ direction with contributions from the lowest-energy mode $n=1$. Furthermore, we let the photon frequency coincide with the low-frequency magnon mode, ω_α. In this case, the magnon-photon coupling simplifies to

$$\mathcal{H}_{\mathrm{CAFM}}=-i\eta\gamma\hbar\sqrt{\frac{NS\hbar\gamma(H_0+H_D)^2\mu_0}{2H_EV}}(p_z-p_z^\dagger)[\alpha+\alpha^\dagger]-\eta\gamma\hbar\sqrt{\frac{NS\hbar\omega_\alpha^2\mu_0}{2\gamma H_EV}}(p_y-p_y^\dagger)[\alpha-\alpha^\dagger], \tag{B18}$$

where we introduce the spatial overlap factor, η.

Notably, both polarizations couple only to the low-frequency magnon mode. Now we can extract the effective coupling constants:

$$\tilde{g}_{x,z,\mathrm{AFM}} = -ig_0\sqrt{2NS}\sqrt{\frac{2\gamma(H_0+H_D)^2}{\omega_\alpha H_E}},$$

$$\tilde{g}_{x,y,\mathrm{AFM}} = g_0\sqrt{2NS}\sqrt{\frac{2\omega_\alpha}{\gamma H_E}}, \tag{B19}$$

where $g_0 = \eta|\gamma|/2\sqrt{\hbar\,\omega_\alpha\mu_0/2V}$. Both coupling constants scale with the number of spins as $\sqrt{N}$, and hence, with the sample size. This is similar behavior to that of collinear antiferromagnets [41] and ferromagnets [5].

APPENDIX C: BACKGROUND CORRECTION AND FIT OF THE AVOIDED LEVEL CROSSINGS

I. BACKGROUND CORRECTION

We perform a one-port VNA calibration at room temperature at the beginning of each measurement. However, at cryogenic temperatures, deviations from the calibration due to temperature-dependent changes in the setup, such as microwave cables, result in a frequency-dependent background. This background can be observed as periodic oscillations in frequency. To remove this background, we use the postprocessing procedure summarized in Fig. 9. Due to the field independence, we subtract the dataset for the lowest applied value of magnetic field and apply a moving average to the data if necessary [Fig. 9(b)]. Notably, if the signal-to-noise ratio is still too low, we use the gradient of the data, which is only done for measurements with the room-temperature setup. In the case of a

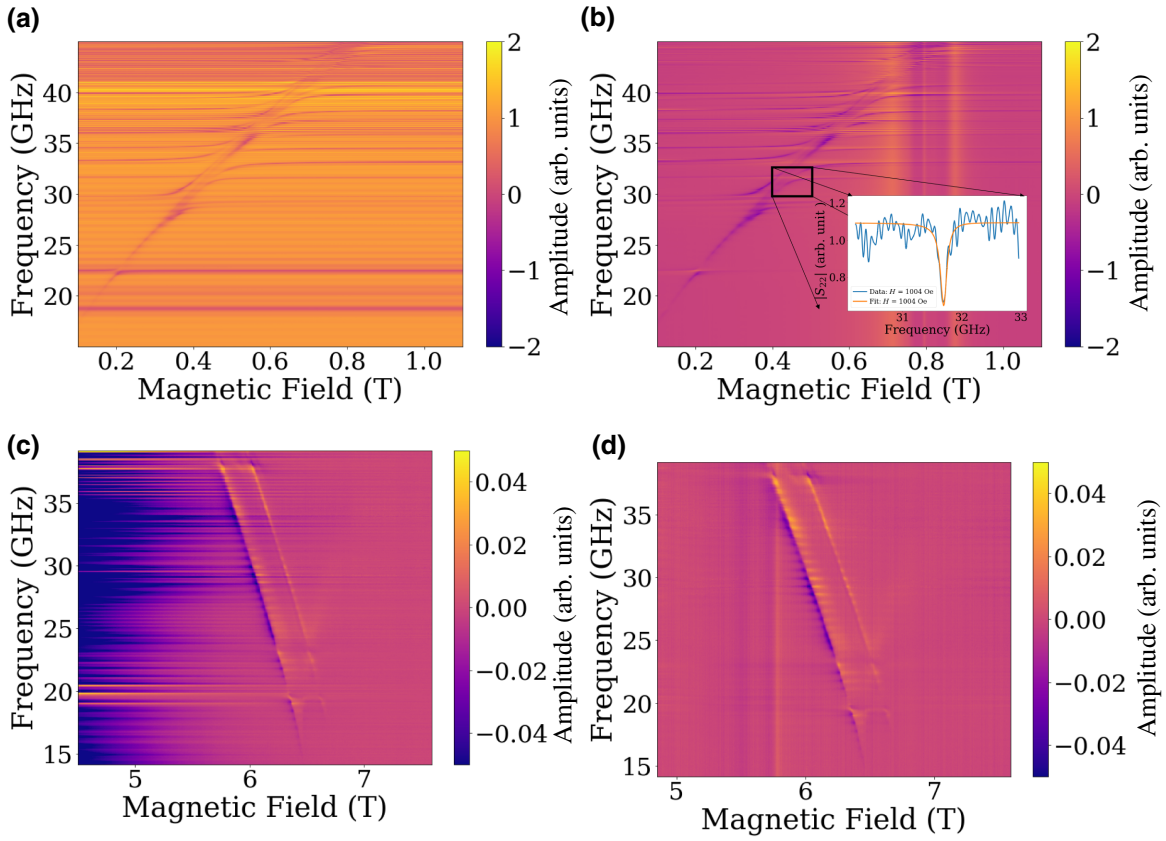

FIG. 9. Mechanisms of the background correction utilized, depending on the signal-to-noise ratio in either the easy-axis or the easy-plane phase. (a) Unprocessed data, including the field-independent oscillations in the spectrum due to standing waves in the involved cables, for instance, measured at 300 K. (b) Background-corrected spectrum via subtracting the spectrum at the highest magnetic field value from the rest of the spectrum. Lines in the anticrossings are artifacts from this subtraction. (c) Background subtraction also displays a linear drift for several datasets, especially for the low-temperature data (here shown for data at 100 K). (d) Linear drift during the field sweep is removed by fitting the linear drift and subsequently subtracting it from data.

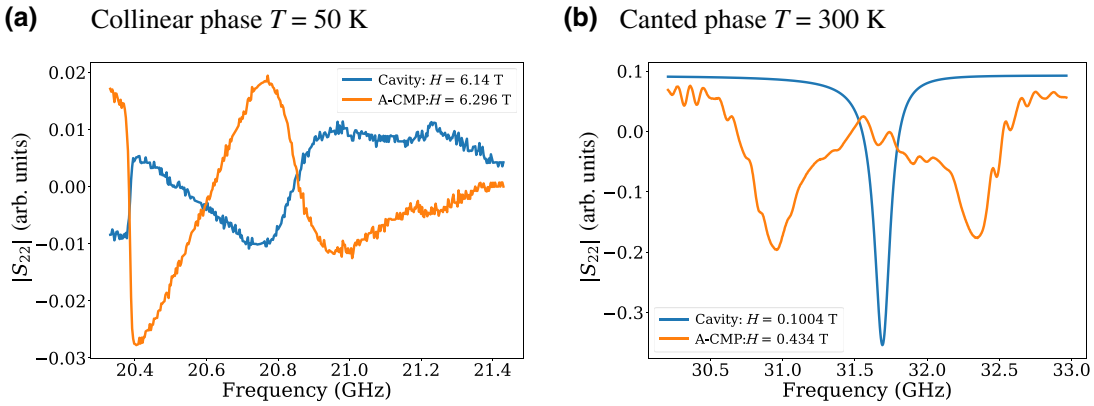

FIG. 10. S_{22} line scans for two representative anticrossings. (a) In the easy-axis phase of hematite at 50 K far from resonance (blue line, corresponding to a magnetic field of 6296 mT) and at resonance (orange line, corresponding to a magnetic field of 6140 mT). (b) In the canted easy-plane phase at 300 K, far from resonance (blue solid line, corresponding to a magnetic field of 120 mT) and at resonance (orange line, corresponding to a magnetic field of 434 mT). Blue lines represent the cavity resonance away from resonant coupling conditions, and the orange line shows the respective line scan under resonant coupling conditions, i.e., where we observe the magnon-photon polariton.

linear drift in frequency as a function of the applied field [Fig. 9(c)], a linear drift is fitted and removed from the spectrum [Fig. 9(d)]. With the postprocessing procedure, we also remove the uncoupled cavity resonance from the resonant region within the avoided level crossing [inset in Fig. 9(b)].

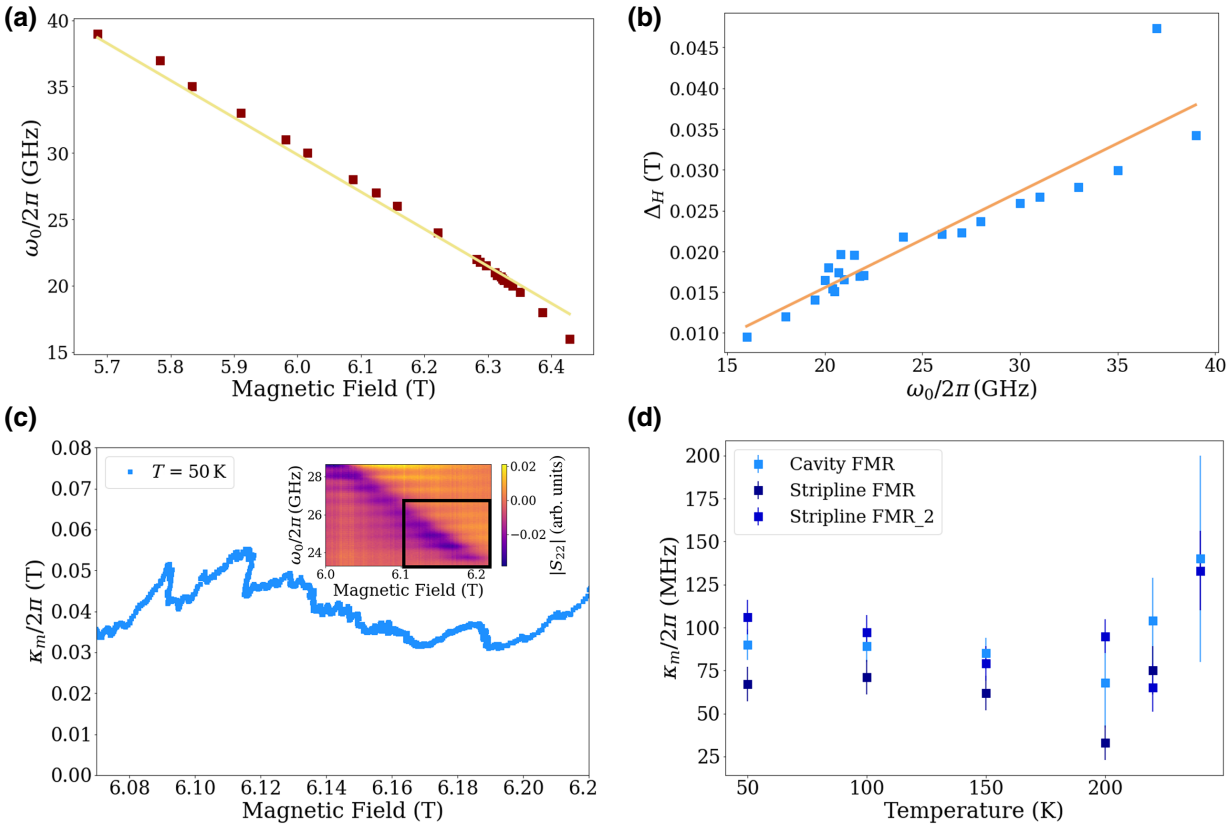

FIG. 11. Determination of magnon linewidth. (a) Frequency and (b) linewidth of the magnon modes obtained by broadband stripline ferromagnetic resonance measurements. (c) Exemplary measurement at 50 K for the magnon linewidth extracted from cavity magnon polariton spectra far away from any anticrossing (rectangular blue). (d) Magnon linewidths as a function of temperature obtained from the two methods. Within the error bars, the linewidths are in good agreement with each other, following the same trend as that observed in Ref. [43].

II. PROCEDURE TO DETERMINE THE COUPLING STRENGTH

To extract the values of the coupling strength, we identify the upper and lower branches of the anticrossing using a peak search. We fit the anticrossing based on the solution of the 2×2 energy eigenmatrix of a system of two coupled harmonic oscillators (photon and magnon). The field dispersion of the magnon follows either that of a collinear easy-axis antiferromagnet or a canted easy-plane antiferromagnet, as described in the main text. From the fit, we also obtain the resonance frequency of the anticrossing, the coupling strength, and a value for the anisotropy field because it is left as a free parameter. The DMI field and the exchange field are kept constant at 2.2 T (extracted from SQUID measurements) and 1000 T, respectively. For the measurements in which we observe multiple anticrossings, we fit each of these anticrossings individually. As a next step to minimize the fitting errors, we average over the obtained values of the free parameters before plotting the resulting fits shown in Figs. 1(b) and 1(d) (black solid lines). The values obtained for the coupling strength are then also used for the determination of the cooperativity.

III. $|S_{22}|$ LINE SCANS FOR ANTICROSSINGS AT 20.8 GHZ ($T < T_{\mathrm{Morin}}$) AND 31 GHZ ($T > T_{\mathrm{Morin}}$)

In addition to the spectra shown in the main text [Figs. 1(b), 1(d) and 2(b)], we also show the line plot of the reflection ($|S_{22}|$) spectra for two different anticrossings at 20.8 GHz at 50 K and (exemplarily) 31.5 GHz at 300 K, respectively, in the collinear and canted phases. This way we can obtain another signature of the strongly coupled ACMP.

In Fig. 10, we show exemplary amplitudes of S_{22} spectra for the uncoupled cavity resonance (blue solid line) and at the avoided anticrossing (at a distance corresponding to $2g$) for these modes. We observe the characteristic presence of two dips (orange solid line), corresponding to the two hybridized branches. Recorded data are only background subtracted, as described in the previous section.

However, there is still a linear amplitude drift in the spectrum, resulting in a slightly different height of the amplitude of each dip under the resonant coupling conditions for the anticrossing. The low-temperature data [Fig. 10(b)] have a decreased signal-to-noise ratio due to changes from the original SOLT calibration at room temperature.

IV. ANALYSIS OF THE SYSTEM COMPONENTS' LINEWIDTHS

A. Magnon linewidth

To accurately determine the magnon dissipation parameter, κ_m, i.e., the linewidth (cf. Fig. 3), we perform stripline ferromagnetic resonance measurements [Figs. 11(a) and 11(b)]. For the deduction of the value from the cavity spectra using the setup shown in Fig. 8(a), we follow the magnon branch far from any cavity resonance or coupling [Fig. 11(c)]. To this end, we use the mean value of these measurements to determine the cooperativity (Fig. 11). Notably, for the two techniques, the linewidths are in good agreement with each other within the error bars [Fig. 11(d)].

B. Cavity-resonator linewidth

The input microwave signal is capacitively coupled to the cavity resonator's volume by placing a pin of a subminiature push-on (SMP) connector matched to 50 Ω to minimize background reflection losses into the antinode of the electric field. Capacitive coupling also avoids an additional perturbation of the cavity's magnetic mode field distribution via microwave driving. The off-resonant loaded quality factor of the main cavity resonance, ω_0, is determined by $Q_c = \omega_0/\Delta\omega_0$, where $\Delta\omega_0 \equiv \kappa_c$, the cavity-resonator linewidth. Figure 12 provides an example of the fitting procedure of the cavity linewidth for the measurement at 50 K.

APPENDIX D: ESTIMATION OF THE COUPLING STRENGTH

I. DETERMINATION OF THE SINGLE-SPIN COUPLING STRENGTH FROM ACMPS

Experimentally, we observe the macroscopic coupling strength, which scales as $\sqrt{N}$ (N contributing spins). However, the measurement of the strength of the interaction in the single (quasiparticle) regime and with respect

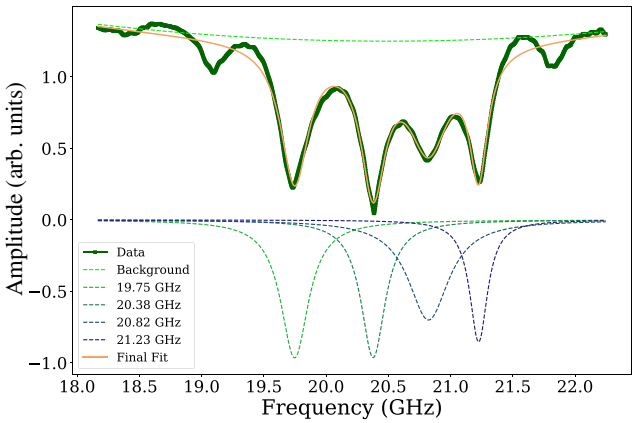

FIG. 12. Determination of the cavity-resonator photon linewidth. Exemplary result measured at 50 K for the simultaneous fitting of multiple Lorentzian functions to determine the correct amplitude and linewidth for the cavity resonance of interest and to remove the experimental setup's background. VNA output power level is set to −6 dBm, as for all measurements on the collinear phase of hematite.

TABLE II. Overview over the single-spin coupling strength and effective macroscopic coupling strength, g', for hematite, including error bars for the investigated resonance from 50 to 300 K.

Mode frequency (GHz)	$g_0/2\pi$ (mHz)	$\Delta g_0/2\pi$ (mHz)	$g'/2\pi$ (MHz)	$\Delta g'/2\pi$ (MHz)
21	123	23	6839	1614
37.5	120	27	6652	1504
40.8	161	80	8917	4428

to on-chip CMPs, with the potential to achieve two-dimensional (2D) systems, is given by the single-spin coupling strength between one photon and one magnon. The calculation of a single-spin coupling strength and a comparison with experimentally observed values also indicates whether the coupling is between a cavity mode and a pure AFM mode. It is also required to check the agreement between our experimental coupling strength, $\tilde{g}_{\mathrm{EA\,or\,CEP}}$, and the analytical formula (Fig. 2 of the main text). Hence, we determine the single-spin coupling strength, $g_0 = \eta|\gamma|/2\sqrt{\hbar\omega_0\mu_0/2V_m}$, of our system. First, the single-spin coupling strength, g_0, is inversely proportional to the mode volume of the cavity modes. Following Ref. [53], the mode volume of a given cavity mode can be derived from the COMSOL® simulations via

$$V_m = \frac{1}{|B_{\max}|^2}\int |B|^2 dV, \tag{D1}$$

where dV corresponds to integration over the entire cavity volume and $B_{\max}$ to the maximal value of the magnetic flux density of the cavity mode. However, typically, there is a deviation from the maximal magnetic field volume and the maximal field value within the sample's volume; this needs to be considered for the correct calculation of the coupling strength, as quantified by the dimensionless mode overlap. In practice, the mode-overlap factor can then be estimated from the different mode volumes via $\eta = \sqrt{V_m^{\mathrm{cavity}}/V_m^{\mathrm{sample}}}$ using the COMSOL® simulations presented in Appendix A. For the principal resonance frequencies at 20.8, 37.5, and 40.8 GHz in our work, we thus obtain mode volumes of about (21.59 ± 5), (22.58 ± 5), and (14.21 ± 5) mm^3, respectively.

Correspondingly, we obtain for the three modes the following overlap factors: $\eta \sim (0.44 \pm 0.02)$ for the mode around 21 GHz, $\eta \sim (0.438 \pm 0.02)$ for 37.5 GHz, and $\eta = (0.466 \pm 0.02)$ for 40.8 GHz. Second, as the coupling strength, g, scales with $\sqrt{N}$, we estimate the number of contributing spins based on the material parameters of hematite.

Hematite arranges in a hexagonal lattice structure with lattice constants $a = 5.03^{-10}$ m and $c = 13.77^{-10}$ m, counting six atoms per unit cell. The iron atoms (spin number $S = 5/2$) contribute to the magnetic moment of hematite and, from density-functional-theory calculations, their magnetic moment yields $3.4 - 4\ \mu_B$/atom [54,55]. As a result, the magnetic moment of hematite (α-Fe_2O_3) amounts to $2 \times 22.2\ \mu_B$/unit cell and, correspondingly, a net spin density of $\rho = 4.95^{22}\ \mu_B/\mathrm{cm}^3$. We thus obtain 6.12^{20} contributing spins, N, for the largest ($5 \times 5 \times 0.5$ mm^3) sample.

The insertion in the expression for g_0 yields exemplary $g_0/2\pi \approx (123 \pm 23)$ mHz and $g'/2\pi \approx (6839 \pm 1504)$ MHz for the mode at 21 GHz, which is used to calculate the analytical curve in Fig. 2(a). All values are summarized in Table II.

II. COUPLING STRENGTH OF FM AND AFM MATERIALS

For a FM system, the macroscopic coupling strength of a CMP reads as

$$\tilde{g}_{\mathrm{FM}} = g'_{\mathrm{FM}} = g_0^{\mathrm{FM}}\sqrt{2N_{\mathrm{FM}}S}, \text{with}$$
$$g_0 = \eta|\gamma|/2\sqrt{\hbar\omega_0\mu_0/2V_m}, \tag{D2}$$

TABLE III. Overview over the calculated ratio from the fitted anticrossings and the corresponding theoretical expectation for data with a resonance frequency of the hematite sample at 29 GHz (mode 2) and 21 GHz (mode 1) at room temperature.

Sample	Mode frequency (GHz)	Coupling strength $g/2\pi$ (MHz)	AFM:FM ratio experiment	AFM:FM ratio theory
YIG ($N_{\mathrm{FM}} = 1.099 \times 10^{19}$)	33	743 ± 75	1.38 ± 0.25	0.811
Hematite ($N_{\mathrm{AFM}} = 6.12 \times 10^{20}$)	29	1025 ± 150		
YIG	23	263 ± 11	0.76 ± 0.04	0.92
Hematite	21	202 ± 4		

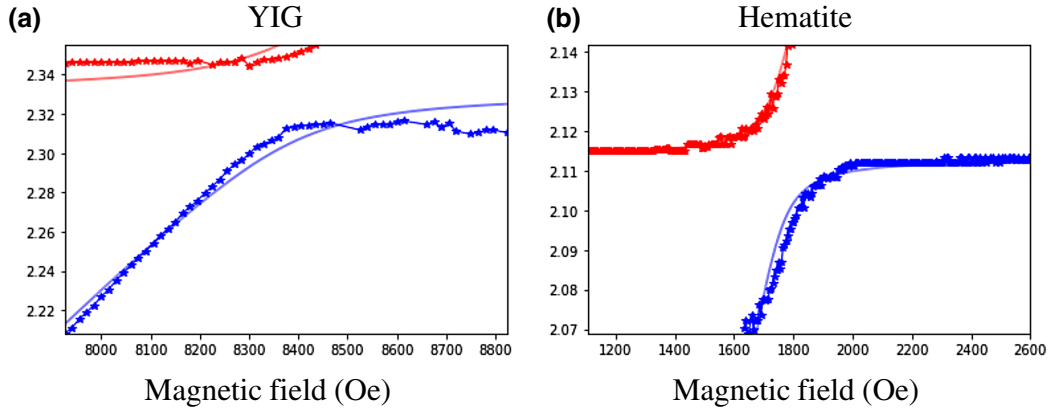

FIG. 13. Illustration of the fitting result for the low-frequency mode at (a) 23 GHz for YIG and (b) at 21 GHz for hematite.

where g_0 is the single-spin coupling strength, ω_0 is the resonance frequency of the CMP, and NS corresponds to the total spin numbers involved in the coupling, as stated in the main text as well.

For a canted antiferromagnet, the coupling strength reads as (see also Table I in the main text)

$$\tilde{g}_{\mathrm{AFM}} \equiv \tilde{g}_{x,z,\,\mathrm{CEP}} \propto g_0^{\mathrm{AFM}} \sqrt{2N_{\mathrm{AFM}}S} \sqrt{\frac{2\gamma(H_0+H_D)^2}{\omega_0 H_E}}. \tag{D3}$$

Therefore, for a given cavity mode (and samples of the same size), the ratio of the coupling strength for a ferromagnet with a canted antiferromagnet yields

$$\frac{\tilde{g}_{\mathrm{AFM}}}{\tilde{g}_{\mathrm{FM}}} = \sqrt{\frac{N_{\mathrm{AFM}}}{N_{\mathrm{FM}}}} \sqrt{\frac{2\gamma(H_0+H_D)^2}{\omega_0 H_E}}. \tag{D4}$$

In Table III, we compare these theoretical predictions with the experimental measurements (see Fig. 2 in the main text and Fig. 6 for a YIG sphere of 1 mm in diameter and a $5 \times 5 \times 0.5\text{-mm}^3$ sample of hematite) and observe clear agreement.

We also show an exemplar fit of CMPs for the mode at 23 (21) GHz for YIG (hematite) in Fig. 13. One must notice the slight shift of frequency of the cavity modes

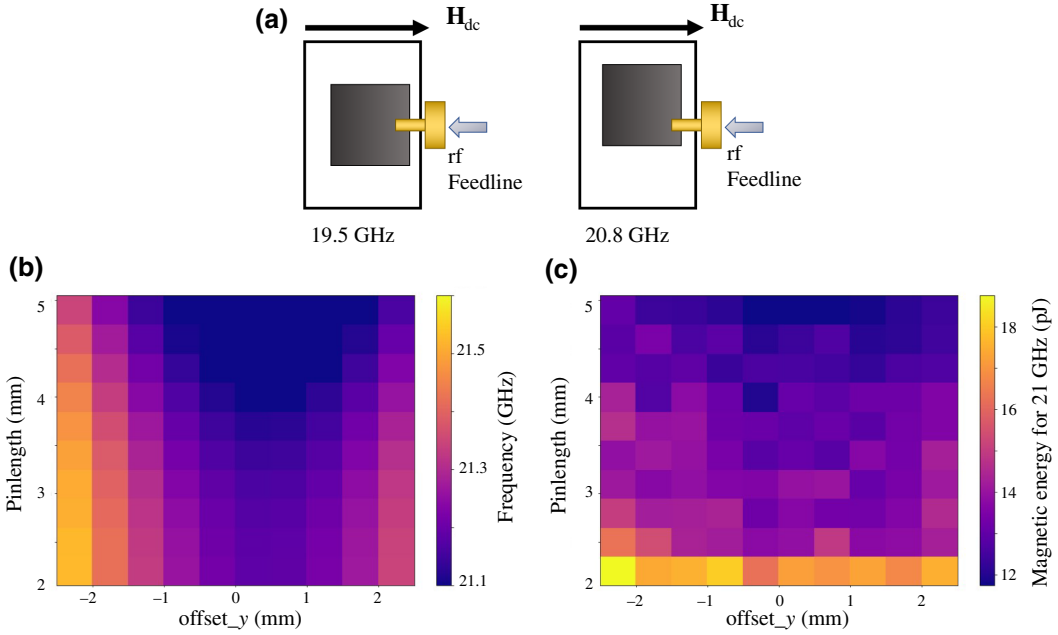

FIG. 14. COMSOL® simulations of the cavity mode at 20.8 GHz for varying sample positions along y and z. (a) Schematics connecting the observed resonance frequency and sample position. (b) Shift of the mode frequency; (c) associated stored magnetic energy. Here, x is set to -1.25×10^{-4} m from zero displacement, corresponding to 0.7 mm from the right border of the cavity volume (cf. Fig. 5).

for the two samples, given the difference in their volumes (factor of 23.9) [56]).

III. IMPACT OF SAMPLE POSITION ON THE FREQUENCY OF CAVITY MODES

To further validate our observations for the collinear phase ($T < T_{\mathrm{Morin}}$), we conduct a second set of measurements to check their sensitivity to the experimental conditions. For two sets of measurements, we observe that the resonance frequency of the mode at 20.8 GHz can shift to 19.5 GHz [cf. Fig. 2(b) of the main text]. We attribute this frequency shift to the fact that we slightly move the sample position, as described below.

For sample sizes that are non-negligible compared to the cavity volume, as here, the frequencies of the cavity modes vary not only with the sample volume (Appendix A) but also slightly with the sample position. To provide evidence of this point, we run COMSOL® simulations where we do vary the position of the sample in the (x, y, z) directions, according to the precision of sample insertion ($\pm 1-2$ mm) (for $\varepsilon \sim 19$ for hematite [7]). As shown on the 2D spectra in Fig. 14, we observe that, for a fixed position in x (e.g., 0.125 mm), the resonance frequency changes by about 300 MHz if the sample is moved by 2 mm in the y direction. A change in height can add a further change by 150 MHz and small shifts in pin insertion as well. A very small change in the x position ($\sim$0.5 mm) can already induce shifts up to 100 MHz.

[1] H. Huebl, C. W. Zollitsch, J. Lotze, F. Hocke, M. Greifenstein, A. Marx, R. Gross, and S. T. B. Goennenwein, High Cooperativity in Coupled Microwave Resonator Ferrimagnetic Insulator Hybrids, Phys. Rev. Lett. **111**, 127003 (2013).

[2] Y. Tabuchi, S. Ishino, T. Ishikawa, R. Yamazaki, K. Usami, and Y. Nakamura, Hybridizing Ferromagnetic Magnons and Microwave Photons in the Quantum Limit, Phys. Rev. Lett. **113**, 083603 (2014).

[3] X. Zhang, C.-L. Zou, L. Jiang, and H. X. Tang, Strongly Coupled Magnons and Cavity Microwave Photons, Phys. Rev. Lett. **113**, 156401 (2014).

[4] X. Zhang, C.-L. Zou, N. Zhu, F. Marquardt, L. Jiang, and H. X. Tang, Magnon dark modes and gradient memory, Nat. Commun. **6**, 8914 (2015).

[5] M. Harder, Y. Yang, B. M. Yao, C. H. Yu, J. W. Rao, Y. S. Gui, R. L. Stamps, and C.-M. Hu, Level Attraction due to Dissipative Magnon-Photon Coupling, Phys. Rev. Lett. **121**, 137203 (2018).

[6] M. Harder, B. M. Yao, Y. S. Gui, and C.-M. Hu, Coherent and dissipative cavity magnonics, J. Appl. Phys. **129**, 201101 (2021).

[7] A. V. Chumak and H. Schultheiss, Magnonics: Spin waves connecting charges, spins and photons, J. Phys. D: Appl. Phys. **50**, 300201 (2017).

[8] B. Bhoi and S.-K. Kim, in *Solid State Physics*, edited by Robert Stamps (Elsevier, 2020), Vol. 71, pp. 39–71.

[9] Y. Tabuchi, S. Ishino, A. Noguchi, T. Ishikawa, R. Yamazaki, K. Usami, and Y. Nakamura, Coherent coupling between a ferromagnetic magnon and a superconducting qubit, Science **349**, 405 (2015).

[10] D. Lachance-Quirion, Y. Tabuchi, S. Ishino, A. Noguchi, T. Ishikawa, R. Yamazaki, and Y. Nakamura, Resolving quanta of collective spin excitations in a millimeter-sized ferromagnet, Sci. Adv. **3**, e1603150 (2017).

[11] D. Lachance-Quirion, S. P. Wolski, Y. Tabuchi, S. Kono, K. Usami, and Y. Nakamura, Entanglement-based single-shot detection of a single magnon with a superconducting qubit, Science **367**, 425 (2020).

[12] S. P. Wolski, D. Lachance-Quirion, Y. Tabuchi, S. Kono, A. Noguchi, K. Usami, and Y. Nakamura, Dissipation-Based Quantum Sensing of Magnons with a Superconducting Qubit, Phys. Rev. Lett. **125**, 117701 (2020).

[13] L. Bai, M. Harder, P. Hyde, Z. Zhang, C.-M. Hu, Y. P. Chen, and J. Q. Xiao, Cavity Mediated Manipulation of Distant Spin Currents Using a Cavity-Magnon-Polariton, Phys. Rev. Lett. **118**, 217201 (2017).

[14] M. Aspelmeyer, T. J. Kippenberg, and F. Marquardt, Cavity optomechanics, Rev. Mod. Phys. **86**, 1391 (2014).

[15] S. V. Kusminskiy, H. X. Tang, and F. Marquardt, Coupled spin-light dynamics in cavity optomagnonics, Phys. Rev. A **94**, 033821 (2016).

[16] T. S. Parvini, V. A. S. V. Bittencourt, and S. V. Kusminskiy, Antiferromagnetic cavity optomagnonics, Phys. Rev. Res. **2**, 022027(R) (2020).

[17] D. Lachance-Quirion, Y. Tabuchi, A. Gloppe, K. Usami, and Y. Nakamura, Hybrid quantum systems based on magnonics, Appl. Phys. Express **12**, 070101 (2019).

[18] D. Zhang, X.-Q. Luo, Y.-P. Wang, T.-F. Li, and J. Q. You, Observation of the exceptional point in cavity magnon-polaritons, Nat. Commun. **8**, 1368 (2017).

[19] J. W. Rao, Y. T. Zhao, Y. S. Gui, X. L. Fan, D. S. Xue, and C.-M. Hu, Controlling Microwaves in Non-Hermitian Metamaterials, Phys. Rev. Appl. **15**, L021003 (2021).

[20] I. Boventer, C. Dörflinger, T. Wolz, R. Machedo, R. Lebrun, M. Kläui, and M. Weides, Control of the coupling strength and linewidth of a cavity magnon-polariton, Phys. Rev. Res. **2**, 013154 (2020).

[21] Y.-P. Wang and C.-M. Hu, Dissipative couplings in cavity magnonics, J. Appl. Phys. **127**, 130901 (2020).

[22] P.-C. Xu, J. W. Rao, Y. S. Gui, X. Jin, and C.-M. Hu, Cavity-mediated dissipative coupling of distant magnetic moments: Theory and experiment, Phys. Rev. B **100**, 094415 (2019).

[23] Y. Yang, J. W. Rao, Y. S. Gui, B. M. Yao, W. Lu, and C.-M. Hu, Control of the Magnon-Photon Level Attraction in a Planar Cavity, Phys. Rev. Appl. **11**, 054023 (2019).

[24] V. Cherepanov, I. Kolokolov, and V. L'vov, The saga of YIG: Spectra, thermodynamics, interaction and relaxation of magnons in a complex magnet, Phys. Rep. **229**, 81 (1993).

[25] C. Hauser, T. Richter, N. Homonnay, C. Eisenschmidt, M. Qaid, H. Deniz, D. Hesse, M. Sawicki, S. G. Ebbinghaus, and G. Schmidt, Yttrium iron garnet thin films with very

low damping obtained by recrystallization of amorphous material, Sci. Rep. **6**, 20827 (2016).

[26] C. Dubs, O. Surzhenko, R. Thomas, J. Osten, T. Schneider, K. Lenz, J. Grenzer, R. Hübner, and E. Wendler, Low damping and microstructural perfection of sub-40 nm-thin yttrium iron garnet films grown by liquid phase epitaxy, Phys. Rev. Mater. **4**, 024416 (2020).

[27] T. Jungwirth, J. Sinova, A. Manchon, X. Marti, J. Wunderlich, and C. Felser, The multiple directions of antiferromagnetic spintronics, Nat. Phys. **14**, 200 (2018).

[28] S. M. Rezende, A. Azevedo, and R. L. Rodríguez-Suárez, Introduction to antiferromagnetic magnons, J. Appl. Phys. **126**, 151101 (2019).

[29] V. Baltz, A. Manchon, M. Tsoi, T. Moriyama, T. Ono, and Y. Tserkovnyak, Antiferromagnetic spintronics, Rev. Mod. Phys. **90**, 015005 (2018).

[30] R. Lebrun, A. Ross, S. A. Bender, A. Qaiumzadeh, L. Baldrati, J. Cramer, A. Brataas, R. A. Duine, and M. Kläui, Tunable long-distance spin transport in a crystalline antiferromagnetic iron oxide, Nature **561**, 222 (2018).

[31] R. Lebrun, A. Ross, O. Gomonay, V. Baltz, U. Ebels, A.-L. Barra, A. Qaiumzadeh, A. Brataas, J. Sinova, and M. Kläui, Long-distance spin-transport across the Morin phase transition up to room temperature in ultra-low damping single crystals of the antiferromagnet α-Fe_2O_3, Nat. Commun. **11**, 6332 (2020).

[32] I. Boventer, H. T. Simensen, A. Anane, M. Kläui, A. Brataas, and R. Lebrun, Room-Temperature Antiferromagnetic Resonance and Inverse Spin-Hall Voltage in Canted Antiferromagnets, Phys. Rev. Lett. **126**, 187201 (2021).

[33] J. Li, C. B. Wilson, R. Cheng, M. Lohmann, M. Kavand, W. Yuan, M. Aldosary, N. Agladze, P. Wei, M. S. Sherwin, J. Shi, Spin current from sub-terahertz-generated antiferromagnetic magnons, Nature **578**, 70 (2020).

[34] P. Vaidya, S. A. Morley, J. van Tol, Y. Liu, R. Cheng, A. Brataas, D. Lederman, and E. del Barco, Subterahertz spin pumping from an insulating antiferromagnet, Science **368**, 160 (2020).

[35] M. Mergenthaler, J. Liu, J. J. Le Roy, N. Ares, A. L. Thompson, L. Bogani, F. Luis, S. J. Blundell, T. Lancaster, A. Ardavan, *et al.*, Strong Coupling of Microwave Photons to Antiferromagnetic Fluctuations in an Organic Magnet, Phys. Rev. Lett. **119**, 147701 (2017).

[36] M. Białek, J. Zhang, H. Yu, and J.-Ph. Ansermet, Strong Coupling of Antiferromagnetic Resonance with Subterahertz Cavity Fields, Phys. Rev. Appl. **15**, 044018 (2021).

[37] K. Grishunin, T. Huisman, G. Li, E. Mishina, T. Rasing, A. V. Kimel, K. Zhang, Z. Jin, S. Cao, W. Ren, *et al.*, Terahertz magnon-polaritons in $TmFeO_3$, ACS Photonics **5**, 1375 (2018).

[38] P. Sivarajah, A. Steinbacher, B. Dastrup, J. Lu, M. Xiang, W. Ren, S. Kamba, S. Cao, and K. A. Nelson, THz-frequency magnon-phonon-polaritons in the collective strong-coupling regime, J. Appl. Phys. **125**, 213103 (2019).

[39] M. Bialek, A. Magrez, and J.-P. Ansermet, Spin-wave coupling to electromagnetic cavity fields in Dysprosium Ferrite, Phys. Rev. B **101**, 024405 (2020).

[40] F. J. Morin, Electrical properties of α-Fe_2O_3 and α-Fe_2O_3 Containing titanium, Phys. Rev. **83**, 1005 (1951).

[41] Ø. Johansen and A. Brataas, Nonlocal Coupling between Antiferromagnets and Ferromagnets in Cavities, Phys. Rev. Lett. **121**, 087204 (2018).

[42] H. J. Fink, Resonance line shapes of weak ferromagnets of the α-Fe_2O_3 and NiF_2 type, Phys. Rev. **133**, A1322 (1964).

[43] R. Lebrun, A. Ross, O. Gomonay, S. A. Bender, L. Baldrati, F. Kronast, A. Qaiumzadeh, J. Sinova, A. Brataas, R. A. Duine & M. Kläui, Anisotropies and magnetic phase transitions in insulating antiferromagnets determined by a spin-Hall magnetoresistance probe, Commun. Phys. **2**, 50 (2019).

[44] C. E. Johnson, L. A. Prelorendjo, and M. F. Thomas, Field induced spin reorientation in orthoferrites $DyFeO_3$, $HoFeO_3$ and $ErFeO_3$, J. Magn. Magn. Mater. **15–18**, 557 (1980).

[45] A. V. Kimel, C. D. Stanciu, P. A. Usachev, R. V. Pisarev, V. N. Gridnev, A. Kirilyuk, and Th. Rasing, Optical excitation of antiferromagnetic resonance in $TmFeO_3$, Phys. Rev. B **74**, 060403 (2006).

[46] H. Watanabe, T. Kurihara, T. Kato, K. Yamaguchi, and T. Suemoto, Observation of long-lived coherent spin precession in orthoferrite $ErFeO_3$ induced by terahertz magnetic fields, Appl. Phys. Lett. **111**, 092401 (2017).

[47] V. M. Judin, A. B. Sherman, and I. E. Myl'nikova, Magnetic properties of $YFeO_3$, Phys. Lett. **22**, 554 (1966).

[48] Z. Jin, Z. Mics, G. Ma, Z. Cheng, M. Bonn, and D. Turchinovich, Single-pulse terahertz coherent control of spin resonance in the canted antiferromagnet $YFeO_3$, mediated by dielectric anisotropy, Phys. Rev. B **87**, 094422 (2013).

[49] K. P. Belov, A. M. Kadomtseva, N. M. Kovtun, V. N. Derkachenko, V. N. Melov, and V. A. Khokhlov, On the character of phase transitions in $ErFeO_3$, Phys. Status Solidi A **36**, 415 (1976).

[50] Y.-P. Wang, J. W. Rao, Y. Yang, P.-C. Xu, Y. S. Gui, B. M. Yao, J. Q. You, and C.-M. Hu, Nonreciprocity and Unidirectional Invisibility in Cavity Magnonics, Phys. Rev. Lett. **123**, 127202 (2019).

[51] D. M. Pozar, *Microwave Engineering*, 4th ed. (Wiley, Hoboken, NJ, 2012).

[52] R. M. White, M. Sparks, and I. Ortenburger, Diagonalization of the antiferromagnetic magnon-phonon Interaction, Phys. Rev. **139**, A450 (1965).

[53] M. M. Denner, 3D Cavity Resonators for Magnon Polariton Experiments, Bachelorthesis; Karlsruhe Institute of Technology (KIT) (2016).

[54] G. S. Parkinson, Iron oxide surfaces, Surf. Sci. Rep. **71**, 272 (2016).

[55] F. Kraushofer, Z. Jakub, M. Bichler, J. Hulva, P. Drmota, M. Weinold, M. Schmid, M. Setvin, U. Diebold, P. Blaha, G. S. Parkinson, Atomic-scale structure of the hematite α-$Fe_2O_3(1\bar{1}02)$ "*R*-cut" surface, J. Phys. Chem. C **122**, 1657 (2018).

[56] M. A. Gilleo and S. Geller, Magnetic and crystallographic properties of substituted yttrium-iron garnet, $3Y_2O_3 \cdot xM_2O_3 \cdot (5-x)Fe_2O_3$, Phys. Rev. **110**, 73 (1958).